Title: Paralemmin-3 sustains the integrity of the lateral plasma membrane and subsurface cisternae of auditory hair cells

Authors: *Victoria C. Halim [1,2], Iman Bahader [2], Dennis Derstroff [3], Christina Ullrich [2,4,5], Makoto F. Kuwabara [3], Greta Hultqvist [6], Kathrin Kusch [2,7], Loujin Slitin [2,4], Lore Becker [8], Martin Hrabè de Angelis [8], Carolin Wichmann [2,4], Dominik Oliver [3], Nicola Strenzke [2], Christian Vogl [1,2,#,*], Manfred W. Kilimann [9,#,*]*

Affiliations:

1. *Auditory Neuroscience Group, Institute of Physiology, Medical University Innsbruck, 6020 Innsbruck, Austria*
2. *Institute for Auditory Neuroscience and InnerEarLab, University Medical Center Goettingen, 37075 Goettingen, Germany*
3. *Institute for Physiology and Pathophysiology, Section for Neurophysiology, Philipps-Universität Marburg, 35037 Marburg, Germany*
4. *Center for Biostructural Imaging of Neurodegeneration, 37075 Goettingen, Germany*
5. *Molecular Medicine Bachelor Program, University Medical Center, 37075 Goettingen, Germany*
6. *Department of Pharmacy, Uppsala University, 75124 Uppsala, Sweden*
7. *Functional Auditory Genomics Group, German Primate Centre, Kellnerweg 4, 37077 Goettingen, Germany and Collaborative Research Center 1690, University of Goettingen, Goettingen, Germany*
8. *German Mouse Clinic, Helmholtz-Zentrum Munich, 85764 Neuherberg, Germany*
9. *Max-Planck-Institute for Multidisciplinary Sciences (City Campus), 37075 Goettingen, Germany*

[#] *these authors contributed equally*

Correspondence:

*Correspondence should be addressed to:

Christian Vogl: christian.vogl@i-med.ac.at or Manfred W. Kilimann: kilimann@mpinat.mpg.de

Keywords:

Cochlear hair cells, membrane scaffolding, cytoskeleton, Spectrin, Prestin

Abstract

In the mammalian inner ear, cochlear inner hair cells (IHCs) enable accurate and faithful synaptic sound encoding, while outer hair cells (OHCs) perform frequency-specific sound amplification and fine-tuning through their intrinsic voltage-dependent somatic electromotility. This latter process is facilitated by the unique trilaminate structure of the OHC lateral wall, which consists of the plasma membrane that is densely occupied by the transmembrane motor protein Prestin, the submembrane actin- and spectrin-based cytoskeleton, and the endomembranous subsurface cisternae. This complex system provides mechanical resilience while allowing for cell expansion and contraction during electromotility. Whereas the ultrastructure of the lateral wall is well described, its molecular architecture remains largely elusive. Here, we identified Paralemmin-3 (Palm3) as a novel protein specifically localized to the lateral walls of auditory HCs to play a crucial role in connecting the plasma membrane to the underlying cytoskeleton and subsurface cisternae. *Palm3*-KO mice display early-onset and progressive hearing impairment that results from diminished cochlear amplification. Subsequent multiscale morphological analyses revealed structural collapse of OHCs that led to progressive and extensive OHC loss along the tonotopic axis. *Palm3*-KO OHCs exhibited disrupted expression and distribution of several membrane-associated proteins – including spectrin isoforms and Prestin – suggesting an essential role of Palm3 in plasma membrane scaffolding. Electron tomography of OHC lateral walls revealed significantly fewer and structurally perturbed subsurface cisternae. Finally, adeno-associated virus (AAV)-mediated rescue of Palm3 during early postnatal development partly restored hearing function, enhanced OHC survival, and restored OHC cell shape as well as membrane protein expression levels. In summary, Palm3 is a key component of the submembrane cytoskeleton in cochlear hair cells, playing a fundamental role in hair cell biology and hearing, and emerges as an attractive candidate for the long-elusive “pillar” component of the hair cell lateral wall ultrastructure.

62 ## Introduction

63 In the mammalian inner ear, two functionally distinct populations of auditory hair cells translate
64 physical sound waves into neural code: whereas inner hair cells (IHCs) faithfully encode sound
65 at their specialized ribbon synapses with afferent spiral ganglion neurons, outer hair cells
66 (OHCs) enable the exquisite frequency discrimination capacity of the mammalian cochlea by
67 actively amplifying basilar membrane motion through their intrinsic voltage-dependent somatic
68 electromotility. The capacity of OHCs to undergo rapid, sub-millisecond length changes
69 requires a delicate balance between radial stiffness and axial compliance to sustain repeated
70 cycles of elongation and contraction without loss of structural integrity during sound
71 transduction (Borkó *et al*, 2005; Batta *et al*, 2003; Hallworth, 1995; He & Dallos, 2000). This
72 equilibrium between flexibility and rigidity is believed to arise from the unique trilaminate
73 architecture of the OHC lateral membrane, which serves as the foundation for the mechanical
74 resilience of OHCs.

75 The OHC plasma membrane (PM) is densely decorated with intramembrane particles
76 – subsequently identified as Prestin motor proteins – that mediate voltage-dependent
77 conformational changes to drive somatic electromotility (Gulley & Reese, 1977; Kalinec *et al*,
78 1992; Zheng *et al*, 2000). Beneath the PM lies the cortical lattice, a meshwork of actin
79 filaments and spectrin cross-links that maintains OHC shape and modulates length and
80 stiffness in response to mechanical forces (Holley *et al*, 1992; Holley & Ashmore, 1988, 1990;
81 Holley, 1996; Legendre *et al*, 2008). Layered underneath the lattice, the subsurface cisternae
82 (SSC) form a circumferential lamellar system (Forge *et al*, 1993), whose cell-biological
83 function is largely unclear but likely includes (i) the maintenance of potential gradients
84 (Spoendlin, 1966), (ii) submembraneous Ca^{2+} homeostasis (Ikeda & Takasaka, 1993; Fuchs
85 *et al*, 2014) and (iii) optimization of motor protein activation (Song & Santos-Sacchi, 2015).
86 Connecting the plasma membrane with the OHC submembrane cytoskeleton are electron-
87 dense structures previously referred to as 'pillars' (Bannister *et al*, 1988; Flock *et al*, 1986;
88 Forge, 1991; Holley *et al*, 1992; Holley & Ashmore, 1988). On ultrastructural level, pillars are

89 regularly spaced (26 ± 11 nm) but vary in length (17-51 nm), orientation, and often bifurcate
90 into a 'Y'-shape at their inner end, with a diameter of 3-4 nm (Forge, 1991; Holley *et al*, 1992;
91 Triffo *et al*, 2019). This structural variability suggests dynamic conformations, consistent with
92 a role as entropic springs within the OHC trilaminate structure (Raphael, 2022). Although first
93 described by electron microscopy in the late 1980s, the molecular identity of the pillars has
94 remained elusive.

95 Paralemmins are a protein family of four isoforms: Paralemmin-1 to Paralemmin-3
96 (Palm1-3) and Palmdelphin (Palmd). In the course of evolution, the paralemmin family
97 appeared with the emergence of vertebrates (Hultqvist *et al*, 2012). The isoforms share a
98 molecular layout consisting of an N-terminal coiled-coil domain and a C-terminal CaaX motif
99 which is lipidated to constitute a membrane anchor. These highly conserved features are
100 connected by intervening sequences which are more divergent between the four isoforms and
101 are predicted to be largely intrinsically unstructured. Early observations suggested an
102 involvement of paralemmins in plasma membrane dynamics and cell shape control (Kutzleb
103 *et al*, 1998). More recently, interactions with the actin cytoskeleton have emerged for Palmd
104 (Kalebic *et al*, 2019; Sáinz-Jaspeado *et al*, 2021), and with spectrin for Palm1 (Macarrón-
105 Palacios *et al*, 2025). Palm1, in particular, was identified as a powerful regulator of the
106 actin/spectrin-based membrane-associated periodic skeleton (MPS) of neuronal axons. The
107 biological roles and molecular properties of Palm2 and Palm3 remain poorly understood.

108 *Palm3*-deficient mice were generated in the context of the EUCOMM mutagenesis
109 programme and were subjected to the phenotyping screen of the German Mouse Clinic
110 (GMC). While homozygous *Palm3*-mutant mice were apparently healthy and fertile, and had
111 normal outcomes in most phenotyping parameters, they displayed reduced startle reflex and
112 pre-pulse inhibition in behavioral testing, and impaired clickbox and auditory brainstem
113 response (ABR) in neurological analysis. These observations suggested hearing impairment,
114 and the gEAR single-cell RNAseq database (Orvis *et al*, 2021) indicated abundant expression
115 of Palm3 mRNA in both populations of cochlear hair cells but in no other cell population of the
116 organ of Corti. Given the marked cell-biological demand of auditory hair cells for durable yet

117 flexible membrane scaffolding, especially in electromotile OHCs, and the recently identified
118 role of Palm1 in organizing the submembrane cytoskeleton and anchoring it to the plasma
119 membrane, we hypothesized that Palm3 might be crucial for the mechanical resilience of hair
120 cells by mediating, or contribution to, the membrane-anchoring of their submembrane
121 skeleton.

122 Therefore, we set out to characterize Palm3 distribution in the murine cochlea and
123 investigated the morphological and functional consequences of *Palm3* deficiency in the
124 peripheral auditory system using systems-physiology, immunohistochemistry, and advanced
125 microscopy techniques – including lightsheet, confocal, 2D-STED nanoscopy, and electron
126 tomography. *Palm3*-KO mice exhibited early-onset, progressive hearing loss due to severe
127 degeneration of auditory hair cells across the entire tonotopic axis. Compatible with a role in
128 membrane scaffolding, Palm3 specifically concentrates in the lateral membranes of both IHCs
129 and OHCs, where it colocalizes with spectrins. *Palm3* loss from OHCs resulted in drastically
130 shortened cell length, reduced spectrins membrane-expression, and compromised
131 subsurface cisternae integrity. Notably, AAV-mediated delivery of wildtype *Palm3* into *Palm3*-
132 KO mice partially restored auditory function, OHC morphology and spectrin localization.

133 In summary, our data identifies *Palm3* as a novel putative deafness gene and Palm3
134 as a promising protein candidate contributing to the proposed ‘pillar complexes’ that link the
135 submembraneous cytoskeleton to the plasma membrane in auditory hair cells.

136

137 # Materials and Methods

138 **Animals**

139 All animal experiments were conducted according to national, regional and institutional
140 guidelines of either the University Medical Center Göttingen, Lower Saxony, Germany or the
141 Medical University Innsbruck, Tyrol, Austria. *Palm3*$^{-/-}$ mice were obtained through either
142 homozygous (*Palm3*$^{-/-}$) or heterozygous (*Palm3*$^{+/-}$) breeding pairs. Wild-type control (*Palm3*$^{+/+}$)
143 mice were obtained from heterozygous (*Palm3*$^{+/-}$) or C57BL/6N breeding pairs. All animals
144 were kept in individually ventilated cages within a specific pathogen-free facility on a 12-h
145 light/dark cycle. Animals were housed in social groups and had unrestricted access to food
146 and water. Male and female mice were included in the study, and no significant sex-based
147 differences were observed.

148

149 **Generation of *Palm3*-KO mice**

150 Palm3-mutant mice were generated in the EUCOMM mutagenesis programme by targeted
151 insertion of a *lacZ* reporter gene, a *neo* selection gene, and an array of *frt* and *loxP* cassettes
152 into introns 1 and 2 of the Palm3 gene of C57BL/6N ES cells. Blastocyst injection of ES cell
153 clone EPD0230_4_A01 at the European Mouse Mutant Archive (EMMA; Monterotondo, Italy)
154 generated the conditional mouse line *Palm3*$^{tm1a(EUCOMM)Wtsi}$. Allele design and availability of
155 mice and materials can be found on the web-page of the International Mouse Phenotyping
156 Consortium (IMPC):
157 https://www.mousephenotype.org/data/alleles/MGI:1921587/tm1a(EUCOMM)Wtsi .
158 Frozen sperm from these mice were imported from EMMA Monterotondo into the Transgenic
159 Facility of the Max-Planck-Institute for Multidisciplinary Sciences (City Campus) and employed
160 for in-vitro fertilization of eggs from transgenic mice expressing Cre recombinase under the
161 control of the EIIa promoter. Deletion of exon 2 together with the *neo* transgene between the
162 two outer-most *loxP* cassettes in founder progeny, generating the constitutive KO allele
163 *Palm3*^{tm1b}, was confirmed by PCR and sequencing. For genotyping, the primer pair 5'-

164 CTCTAAGTCCACAACTAGGCAGGA-3' (Sense_Upstream-Exon2-38212) and 5'-
165 GCTTGACCCCAATTGTGC-3' (Asense_Upstream-Exon2-38213) detects the WT allele (340
166 bp amplimer), whereas the primer pair 5'-CACTGCATTCTAGTTGTGGTTTGT-3'
167 (Sense_SV40pA_03822) and 5'-GAGCTTGGGTTGCACTGGTC-3' (Asense_Downstream-
168 Exon2-38214) detects a 146 bp KO amplimer after deletion of the *neo*/exon2 sequence block.
169 Exon 2 deletion causes a reading-frame shift but retains the *lacZ* reporter cassette. The EIIa-
170 *Cre* transgene was subsequently bred out, and the colony was maintained in the C57BL/6N
171 background.
172
173 **Auditory systems physiology**
174 ABR and DPOAE measurements were performed as previously described (Jing *et al*, 2013;
175 Strenzke *et al*, 2016; Pauli-Magnus *et al*, 2007). ABR and DPOAE measurements for the initial
176 phenotype description of *Palm3*-KO were performed in 3-week- and 12-13-week-old *Palm3*-
177 KO and WT littermates, whereas measurements for *Palm3*-rescue experiments were
178 performed in AAV-injected 5–6-week-old *Palm3*-KO mice. Animals were anesthetized by
179 intraperitoneal injection of ketamine (125mg/kg) and xylazine (2.5 mg/kg). The heart rate was
180 continuously monitored throughout the procedure. A rectal temperature-controlled heat
181 blanket (Hugo Sachs Elektronik–Harvard Apparatus) was used to maintain a constant core
182 temperature of 37℃. Stimulus generation, presentation, and data acquisition was carried out
183 using the TDT Systems III operated by BioSig32 software (Tucker Davis Technologies).
184 Acoustic stimulus in form of either 12 ms tone-burst (10 ms plateau, 1 ms cos2 rise/fall) or
185 clicks of 0.03 ms were presented ipsilaterally at a stimulation rate of 40 Hz and 20 Hz,
186 respectively, at frequencies of 4, 6, 8, 12, 16, 24, and 32 kHz in the free field using a JBL 2402
187 speaker (JBL GmbH & co, Neuhofen, Germany). ABRs were recorded by placing
188 subcutaneous needle electrodes at the vertex and near the mastoid region, with a ground
189 electrode positioned dorsally near the base of the tail. The difference potential between the
190 recording electrodes was amplified (50,000x using a custom-built JHM NeuroAmp 401
191 amplifier), filtered (0.4-4 kHz), and averaged over 1300 sweeps to generate two mean traces

192 per sound intensity. Recording contaminated by noise, primarily due to ECG interference,
193 were automatically excluded using the artifact rejection function in BioSig32. Click ABRs were
194 measured in 10 dB SPL steps. ABR threshold was subjectively determined as the lowest
195 stimulus intensity eliciting a consistent waveform in both averaged traces and were validated
196 by an independent observer. ABR peaks were manually assigned according to their normal
197 latency values, and each wave amplitude was calculated as the difference between highest
198 point of the wave and the subsequent local minimum. In rescue experiments, recordings were
199 first performed on the AAV-injected (ipsilateral) ear of *Palm3*-KO mice, then occluded using
200 electrode gel and tissue to induce a 30-40 db conductive hearing loss (Pauli-Magnus *et al*,
201 2007) to avoid acoustic crosstalk for the subsequent measurements in the non-injected
202 (contralateral) ear. Tone burst thresholds that surpassed 80 dB were assigned as 90 dB for
203 the purpose of calculating means and SEMs. For DPOAE measurements, two continuous sine
204 wave stimuli (f1, f2) were generated using Tucker-Davis system III and ED1/EC1 speaker
205 system (Tucker-Davis). A custom-built ear probe was employed to deliver two primary tones
206 into the ear canal and to record DPOAEs using a miniature microphone (MKE-2, Sennheiser,
207 Hannover, Germany). The microphone signal was amplified via an external sound card
208 (Terratec DMX 6Fire USB) and digitized with a TDT III system. All systems-physiological
209 experiments were performed in compliance with the national animal care guidelines and were
210 approved by both the board for animal welfare of the University Medical Center Göttingen and
211 the State Animal Welfare office of Lower Saxony (AZ19/3133).
212
213 **Immunohistochemistry**
214 Cochleae were fixed with 4% FA in PBS for 1h on ice. Apical turns of the organ of Corti were
215 dissected out of the cochleae and treated with 0.5% Triton-X100 in PBS for permeabilization.
216 This was followed by a blocking step using a PBS-based blocking buffer (BB) containing 0.5%
217 Triton-X100 and 10% goat serum for 1h at RT. Subsequently, samples were incubated
218 overnight with primary antibodies diluted in BB. The following primary antibodies were used:
219 mouse anti-alpha2 Spectrin (SH3-domain, #803201, Biolegend), mouse anti-beta1 Spectrin

220 (aa 1555-2137, #75-374, Antibodies inc), mouse anti-beta2 Spectrin (aa 2101-2189, #612562,
221 BD Transduction Laboratories™), chicken anti-Calretinin (#214 106, Synaptic Systems),
222 mouse anti-HuD (H-9) (#sc-48421, Santa Cruz), mouse anti-Myosin7a (#MYO7a 138-1,
223 Developmental Studies Hybridoma Bank), guinea pig anti-Parvalbumin (#195 004, Synaptic
224 Systems), and rabbit anti-Prestin (#ab242128, Abcam). The next day, secondary antibodies
225 and/or nanobodies were added to the samples. The following secondary antibodies were
226 used: anti-GFP FluoTagX4 Atto488 (#N0304- At488-L, NanoTag), anti-mouse FluoTagX2
227 IgG1 488 (#N2002-At488, NanoTag), anti-mouse FluoTagX2 IgG1 635p (#N2002- Ab635p,
228 NanoTag), anti-mouse FluoTagX2 IgG1 565 (#N2702-At565s, NanoTag), anti-mouse
229 FluoTagX2 IgG2a/b 635p (#N2702- Ab635p-S, , NanoTag), anti-rabbit FluoTagX4 580
230 (#N2404- Ab580-S, NanoTag), anti-rabbit FluoTagX4 635p (#N2404-Ab635p, NanoTag), goat
231 anti-chicken 488 (#A11039, Invitrogen), goat anti-guinea pig 488 (#A-11073, ThermoFisher
232 Scientific), goat anti-mouse IgG STAR580 (#ST580-1001, Abberior), goat anti-rabbit
233 STAR635p (#ST635P-1002, Abberior), TO-PRO™-3 Iodide 642/661 (#T3605, ThermoFisher
234 Scientific). Depending on the specific acquisition system used, samples were then mounted
235 using either ProLongTM Glass Antifade Mountant (#P36984, Life Technologies Corporation)
236 or Mowiol mounting medium (#0713, Carl Roth GmbH + Co. KG).
237
238 **Palm3 antibodies**
239 As immunogens, two mouse Palm3 sequences were selected that are non-overlapping, and
240 do not contain sequence stretches with similarity to the other paralemmin isoforms (i.e., they
241 exclude the N-terminal coiled-coil region and the C-terminal CaaX motif): Palm3-p31 (aa 114-
242 399; QSAST…GEASWE) and Palm3-p32 (aa 404-725; VEKVE…ASGPK). These inserts
243 were amplified by RT-PCR from mouse brain RNA, cloned into the SmaI site of pQE-82L, and
244 verified by sequencing (RefSeq XP_486140). His-tagged fusion proteins were expressed in
245 bacteria and affinity-purified on nickel-agarose. As both fusion proteins were partially
246 insoluble, affinity purifications were performed on the native, soluble fractions as well as on
247 the denatured, urea-solubilized fractions, following Qiagen protocols. Rabbits were immunized

248 separately with native and denatured immunogens at Pineda-Abservice (Berlin, Germany),
249 and sera were affinity-purified on the respective CNBr- or tresyl-agarose-coupled immunogen
250 proteins. Antibody preparations anti-Palm3 p31 rb2 nat (fr2-3), anti-Palm3 p32 rb1 den, and
251 anti-Palm3 p31 rb1 den (fr2-3) were employed in the present study as indicated.
252
253 **Lightsheet microscopy**
254 Cytocochleograms were performed in hearing animals at p21. Following overnight fixation in
255 4% FA in PBS at 4°C, osseous labyrinths were decalcified at RT for four days in 10% EDTA.
256 Chemical tissue clearing and immunolabeling were performed using a modified version of the
257 iDISCO+ protocol (Renier *et al*, 2016; Rankovic *et al*, 2021).
258 All incubation and washing steps were performed on a thermomixer at 37°C and at RT,
259 respectively. After permeabilization and blocking, a mixture of the primary antibody rabbit anti-
260 Myosin7a (#PTS-25-6790-C050, Enzo) and nanobody anti-rabbit FluoTagX4 IgG 635p
261 (#N2404-Ab635p, NanoTag) was prepared and preincubated for 45 min at RT. The primary
262 antibody/nanobody mixture was then diluted in blocking solution and applied to the samples
263 for 6 days. After washing, samples were cleared in 66% dichloromethane (#270997, Sigma-
264 Aldrich)/33% methanol for 3 h at RT, followed by 2 x 15 min incubation in 100%
265 dichloromethane, and stored in dibenzyl ether (#33630, Sigma-Aldrich). Imaging was
266 performed using a LaVision UltraMicroscope II (NA 0.154, sheet thickness 5 µm) with 3 µm
267 step size and 8-10x total zoom (2x objective, 4-5x optical zoom). OHC survival along the
268 tonotopic axis was analyzed using a custom MATLAB script (Rankovic *et al*, 2021)
269 implementing Greenwood's function (Greenwood, 1961) to map frequency regions (4, 8, 12,
270 16, 24 and 32 kHz) based on mouse cochlear parameters (Müller *et al*, 2005). OHCs were
271 manually counted using the Cell Counter tool in ImageJ/Fiji (Schneider *et al*, 2012) in respect
272 to their approximate frequency regions.
273

274 **OHC length and fluorescence intensity analysis**

275 OHC lengths were measured using the straight-line tool in ImageJ/Fiji (Schneider *et al*, 2012).
276 Fluorescence intensities of Palm3, Prestin, and αII-Spectrin were quantified from maximal
277 projections of sample images in ImageJ/Fiji (Schneider *et al*, 2012). Background fluorescence
278 was measured in a 3 µm x 3 µm area lacking apparent fluorescence intensity, subtracted from
279 the image, and average intensities within 50 µm x 50 µm regions containing OHCs were then
280 measured. Average intensity values were normalized to control.

281 To quantify spectrin fluorescence intensities in WT, *Palm3*-KO, and *Palm3*-rescue animals,
282 OHC masks were generated in *Imaris* 10.2.0 using the *cells* algorithm, based on Myosin7a
283 staining (filter width: 0.8 µm; largest sphere diameter: 3 µm). Masks were expanded to include
284 membranes, and adjacent cells were split using a 6.0 µm diameter threshold. The resulting
285 3D reconstructions were exported to *surfaces* for average fluorescence intensity analysis.
286 Cuticular plate intensities were analyzed by creating 3D *surfaces* renderings from spectrin
287 staining (surface detail: 0.3 µm; largest sphere diameter: 0.4 µm). All average intensity values
288 were normalized to controls.

289

290 **Patch-clamp electrophysiology on OHCs**

291 Animal care and tissue collection from *Palm3*-KO and wildtype mice followed federal and
292 institutional guidelines at the Philipps University Marburg. Mice of the indicated age were killed
293 by decapitation under isoflurane anesthesia. Cochleae were dissected on ice in a solution
294 containing (in mM) 144 NaCl, 5.8 KCl, 1.3 $CaCl_2$, 0.9 $MgCl_2$, 10 HEPES, 0.7 Na_2HPO_4, 5.6
295 glucose (pH adjusted to 7.4 with NaOH). Recordings were done within 2 hours after dissection.
296 For patch-clamp recordings, pieces of the apical cochlear turn were mounted in a recording
297 chamber with a flexible glass fiber glued to the bottom coverslip at one end. The bath chamber
298 was continuously perfused with the same extracellular solution used for dissection. For
299 establishing whole-cell patch-clamp recordings, the preparation was viewed with an upright
300 BX51WI microscope equipped with water immersion objectives (Olympus, Tokyo, Japan).
301 Whole-cell patch-clamp recordings were performed with EPC10 amplifiers (Heka, Lambrecht,

302 Germany) controlled by Patchmaster software (Heka). Patch pipettes were pulled from
303 borosilicate glass to obtain open tip resistances of 2-4 MOhm when filled with intracellular
304 solution. All experiments were performed at room temperature (21-23°C).
305
306 **Non-linear capacitance measurements**
307 Recording pipettes were filled with intracellular solution containing (mM): 100 CsCl, 20 TEA-
308 Cl, 3.5 $MgCl_2$, 0.1 $CaCl_2$, 6 BAPTA, 2.5 Na_2ATP, 5 HEPES (pH adjusted to 7.4 with NaOH,
309 Osmolarity adjusted to 300 mOsm/kg with glucose). Whole-cell series resistance was < 10
310 MOhm. NLC was measured using a stair-step protocol as described (Oliver *et al*, 1998; Huang
311 & Santos-Sacchi, 1993), with a step duration of 10 ms at voltage increments of 10 mV.
312 Currents were low-pass filtered at 10 kHz and sampled at 100 kHz. In these experiments,
313 whole-cell membrane capacitance (C_M) was not compensated. The time constant of current
314 decay (t) was determined from mono-exponential fits to the current transients, and input
315 resistance (R_{in}) was calculated from steady-state currents at the end of each voltage step.
316 Integration of the current transients yielded the charge (Q). Cm(i) at each incremental voltage
317 step i was derived according to (Huang & Santos-Sacchi, 1993), taking into account the
318 relatively low Rm of OHCs:
319
320 $$C_M(i) = (R_{in}/R_m)^2 (Q/V_C)$$
321
322 and
323
324 $$R_{in} = R_M + R_s$$
325
326 $$R_S = (R_{in}\ t\ V_C)$$
327

328 R_S is the series resistance; R_M is the membrane resistance and V_C is the command voltage
329 step amplitude (10 mV). C_M (i) was plotted versus (V(i) + V(i + 1))/2, after correction of all
330 voltages for series resistance errors.
331
332 Voltage-dependent capacitance was fitted with a derivative of the Boltzmann function:
333
334 $$C(V_M) = C_{lin} + (Q_{max} / (a \exp((V_M - V_{1/2}) / a) (1 + \exp((V_M - V_{1/2}) / - a))^2)$$
335
336 where C_{lin} is the linear membrane capacitance, V_M is the membrane potential, Q_{max} is the
337 maximum voltage sensor charge moved through the membrane electrical field, $V_{1/2}$ is the
338 voltage at half-maximal charge transfer, and a is the slope factor of the voltage-dependence.
339 C_{lin} reflects the surface membrane area of OHCs. As a measure for prestin density in the OHC
340 membrane, NLC is also presented normalized to C_{lin}.
341
342 **Polymer resin (melamine) embedding**
343 Melamine was prepared following the protocol described in (Revelo *et al*, 2014). Briefly, 48
344 mg of *p*-toluenesulfonic acid monohydrate (#402885, Sigma Aldrich) was dissolved in 0.576
345 mL distilled water, followed by the addition of 1.344 g 2,4,6-Tris[bis(methoxymethyl)amino]-
346 1,3,5-triazine (#T2059, TCI chemicals) and vortexed for 2 h until completely dissolved. After
347 fixation and immunostaining, each organ of Corti was placed into the head of a block mold
348 (#E69931, Easy-Molds™) and 100 µL of freshly prepared melamine was poured inside the
349 mold until the organ of Corti was covered. To facilitate melamine penetration into the tissue,
350 samples were incubated overnight at RT in a vacuum desiccator. Melamine was polymerized
351 at 40°C for 24 h. Subsequently, the block mold was filled up with Epoxy resin (#40200029,
352 EpoFix kit, Struers) and cured at 60°C for 48 h. Melamine blocks were sectioned into ~80-90
353 nm ultra-thin sections using a Reichert Ultracut S microtome (Leica Microsystems, Vienna,

354 Austria) with a diamond knife (Diatome Ultra 45°, Switzerland, Nidau) at 3-6° clearance angle.
355 Sections were mounted in Mowiol for 2D stimulated emission depletion (STED) microscopy.
356
357 **Li's intensity correlation quotient (ICQ) and nearest neighbor distance (NND) analysis**
358 STED images were pre-processed to subtract background fluorescence in ImageJ/Fiji
359 software (Schneider *et al*, 2012). A 3 µm x 3 µm area lacking apparent fluorescence intensity
360 was measured to determine average background intensity, which was then subtracted from
361 the image. ICQ values obtained using Li's intensity correlation analysis (ICA; Li *et al*, 2004)
362 using the Colocalization Analyzer on Huygens Professional software (Scientific Volume
363 Imaging, Hilversum, The Netherlands). Nearest neighbor distances (NND) of Palm3
364 immunolabeling were analyzed in *Imaris* 10.2.0 (Oxford Instruments) using the spot-detection
365 algorithm with an estimated XY diameter of 0.08 µm. Thresholding based on the average
366 Palm3 signal intensity was applied to remove noise, and the few detected spots that were not
367 localized within the cells of interest were manually excluded. NND was calculated from the
368 shortest distance between the centers of homogeneous masses of detected spots. Figure 6A
369 was deconvolved for representation purposes with Huygens Professional version 25.04 using
370 the "Standard" Deconvolution Express Profile with Acuity set to: -5.3 (Scientific Volume
371 Imaging, The Netherlands).
372
373 **High pressure freezing and freeze-substitution**
374 High pressure freezing (HPF) and freeze-substitution (FS) and embedding in epoxy resin
375 (EPON) were essentially carried out as described in (Wong *et al*, 2014; Chakrabarti *et al*,
376 2018, 2022). For HPF, apical organs of Corti were placed within a type A aluminum specimen
377 carrier (Leica Microsystems, Wetzlar, Germany) with a depth of 0.2 mm, filled with HEPES-
378 HBSS NaCl 141.7, HEPES 10, KCl 5.36, $MgCl_2$ 1, $MgSO_4$*7H_2O 0.5, freshly added: glucose
379 2 mg/ml and L-glutamine 0.5 mg/ml (pH adjusted to 7.2 with NaOH. Osmolarity ≤ 300
380 mmol/kg). A type B carrier was dipped into 1-hexadecene (Sigma-Aldrich, Darmstadt,
381 Germany) and positioned adjacent to the sample. The samples were promptly frozen using

382 the HPM100 (Leica Microsystems, Wetzlar, Germany) and directly placed in liquid nitrogen
383 for storage. For FS, the EM AFS2 (Leica Microsystems, Wetzlar, Germany) was utilized.
384 Samples were incubated in 0.1% (w/v) tannic acid in acetone for four days at -90°C. Samples
385 were washed three times with acetone for 1 h each. Thereafter, 2 % (w/v) osmium tetroxide
386 in acetone was added and incubated for 7 h. The temperature was increased in incremental
387 steps of 5°C per hour to -20°C. At -20°C, samples were incubated for another 17 h before the
388 temperature was raised to 4°C in 10°C increments per hour. While the samples were being
389 heated to room temperature, they were washed on three occasions with acetone, each for
390 1 h. Following the washing process, the samples were infiltrated with 1:1 EPON (Agar pre-mix
391 kit, Plano GmbH, Wetzlar, Germany) in acetone solution and incubated for 3-6 h. The solution
392 was replaced with 100% EPON and incubated overnight. Then, EPON was replaced with fresh
393 EPON and incubated for an additional 3-6 h. All incubation steps were conducted on a rotary
394 wheel at RT. Subsequently, the samples were positioned within embedding molds (Agar
395 Scientific Ltd., Stansted, Essex, United Kingdom), filled with 100% fresh EPON, and
396 polymerized in an incubator (Incu-line, VWR, Darmstadt, Germany) set to 70°C for 48 h.
397 Samples that did not exhibit the desired orientation following embedding were reoriented in
398 order to allow for the acquisition of a cross-section through the organ of Corti (in the region of
399 the apical 1.5 turns). The portion of the EPON containing the sample was sectioned with a
400 saw, placed in embedding molds (Agar Scientific Ltd., Stansted, Essex, United Kingdom)
401 oriented as desired, filled with EPON, and polymerized for 48 h at 70°C in the drying oven
402 Incu-line (VWR, Darmstadt, Germany). For this purpose, the AGR1140 Agar 100 Premix Kit –
403 Hard (Agar Scientific, London, United Kingdom) was used. The EPON directly surrounding
404 the sample was roughly trimmed using a file (Titania Solingen GmbH, Wülfrath, Germany) and
405 a razor blade (Plano GmbH, Wetzlar, Germany) into the shape of a trapezoid and
406 subsequently smoothened at the block face with the Cyrotrim 45° (DiATOME, Nidau,
407 Switzerland) in the EM UC7 ultramicrotome (Leica Microsystems, Wetzlar, Germany).
408 Following the trimming of the samples, 75 nm ultrathin sections were obtained for transmission
409 electron microscopy (TEM) analysis of the immunogold label and 2D analyses. This was

410 achieved by approaching the block face with a 35° diamond knife (DiATOME, Nidau,
411 Switzerland) using the EM UC7 ultramicrotome (Leica Microsystems, Wetzlar, Germany). For
412 each sample, a total of 3-5 sections were applied onto 17-45 1 x 2 mm copper slot grids (3.05
413 mm Ø; Plano, Germany) coated with 1% formvar (w/v in water free chloroform). For electron
414 tomography (ET), 250 nm semithin sections were generated and 3-5 sections were applied to
415 20-35 75 copper mesh grids (3.05 mm Ø; Plano, Germany), which were coated with 1%
416 formvar.
417 Both the grids for TEM as well as for ET analysis were stained by incubating them on droplets
418 of Uranyless (lanthanum, gadolinium and dysprosium salts in distilled water, Delta
419 Microscopies, Mauressac, France) for 20 to 25 minutes. Subsequently, the grids were washed
420 six times on droplets of distilled water, for one minute each. For ET samples, droplets of 10
421 nm gold nanoparticles (10 nm gold colloid, BBI solutions, Freiburg, Germany) were applied to
422 the mesh grids for ET by incubating from both sides for 8 minutes each. The gold nanoparticles
423 serve as fiducials for tomogram alignment.
424
425 **Transmission electron microscopy**
426 TEM examination for comparison of the abundance of SSC employed the JEM 1011 TEM
427 (JEOL, Freising, Germany). For each sample one to four grids were examined and 2D
428 micrographs of OHC were obtained at different magnifications. Overview micrographs of the
429 examined cochlear region were taken at 800-fold magnification to determine whether the cells
430 are indeed OHC. Micrographs of the individual OHC were obtained at 2,500-fold magnification
431 and close-ups of the plasma membrane of each OHC in the region of nucleus at 6,000-fold
432 magnification.
433 Only OHCs that were unambiguously identified as such, based on their localization and
434 morphology, were examined. Therefore, stereocilia had to be in close proximity to the cells
435 and the tunnel of Corti as well as the IHC and cochlear nerve fibers had to lie medial to the
436 cells. Since the region of interest (ROI) was the plasma membrane in the region lateral to the

437 nucleus, only OHC with a visible nucleus were imaged. The final criterion was the integrity of
438 the plasma membrane to ensure a near-native state of the OHC.
439
440 **Electron tomography**
441 Single tilt series of the area lateral to the nucleus of the OHC was acquired using the Serial-
442 EM software package (Mastronade, University of Colorado, USA) (Kremer *et al*, 1996a) at a
443 JEM 2100Plus TEM (JEOL, Freisingen, Germany) essentially performed as described in
444 (Hintze *et al*, 2024). This TEM is equipped with a Xarosa camera (EMSIS GmbH, Münster,
445 Germany) and the RADIUS software package (EMSIS GmbH, Münster, Germany), used for
446 finding the ROI, and operates at 200 kV. The tilt series, if possible, spanned a range of 1°
447 increments from -55 to +55° and were obtained at either 12,000x or 20,000x magnification.
448 Subsequently, tomograms of the OHC were generated using the IMOD software package
449 etomo (Mastronade, University of Colorado, USA) (Kremer *et al*, 1996b). In this process, one
450 pixel corresponded to a distance of 1.758 nm at a 12,000-fold magnification and of 1 nm at
451 20,000-fold magnification.
452
453 **Analysis of SSC-TEM data**
454 2D micrographs obtained via TEM at 6,000-fold magnification were used to quantify alterations
455 in the number of SSC between WT and *Palm3*-KO mice. For this purpose, the plasma
456 membrane lateral to the nucleus of each OHC was traced and the length was measured using
457 the “freehand line” tool in the Fiji ImageJ software (Schindelin *et al*, 2012). Pixels were
458 converted into nanometers by measuring the scale bar in 6000x magnified micrographs using
459 the straight-line tool to determine a conversion factor, with one nanometer corresponding to
460 approximately 0.95 pixels. To determine the number of SSC per micrometer of plasma
461 membrane, the SSC in the ROI of each OHC were enumerated.
462
463 **Analysis of SSC-ET data**

464 Distinguishable SSC on each virtual section of each tomogram were sculpted manually on
465 their membrane, using the “sculpting” tool of the IMOD 3dmod software package etomo
466 (Mastronade, University of Colorado, USA) (Kremer *et al*, 1996b). The SSC belonging to a
467 single tomogram were treated as a closed object and meshed into a 3D model without a cap.
468 For this object, the overall surface area of the mesh, as well as the total volume of the outline
469 and the volume within the mesh, were determined.
470 In order to put the position of the SSC within the OHC into perspective, the plasma membrane
471 of the OHC lateral to the nucleus and the mitochondria, when present, were incorporated into
472 the 3D models. The plasma membrane and the mitochondria were manually sculpted on every
473 third virtual section and transferred to the sections in between using the “interpolator” tool in
474 IMOD 3dmod (Mastronade, University of Colorado, USA) (Kremer *et al*, 1996b), provided that
475 their course exhibited only slight variations. Otherwise, the procedure described for the SSC
476 was employed.
477 To facilitate quantitative comparison of the localization of the SSC between the WT and
478 *Palm3*-KO mice, the shortest distance between the outer SSC membrane and the inner border
479 of the plasma membrane of the OHC was determined on the virtual sections of the tomograms
480 using the “measuring” tool in IMOD 3dmod (Mastronade, University of Colorado, USA)
481 (Kremer *et al*, 1996b). Consistency and reliability of the results was ensured, by measuring
482 this distance between the SSC and the plasma membrane nine times for each tomogram at
483 different positions. The initial three measurements were obtained from the virtual section that
484 marked the midpoint of the entire series. In this instance, the shortest distance was determined
485 for the SSC situated at the middle of the section as well as for the SSC located at either ends.
486 Measurements were repeated on the 50th section above and below the central section for the
487 tomograms obtained at 20,000x magnification and on the 20th section above and below for the
488 tomograms obtained at 12,000x magnification.
489
490 **rAAV expression construct and viral vector production**

491 A fusion cDNA encoding yellow fluorescent protein (YFP) and mouse Paralemmin-3 (from
492 codon 2 [ALQTP…] to the stop codon), connected by the 20 aa linker
493 GSSPSTSLYKKAGSAAAPFT, was originally cloned into Invitrogen Vivid Colors pcDNA6.2/N-
494 YFP-DEST. This fusion cDNA was subcloned, by InFusion cloning (TAKARA) according to
495 the manufacturer's instructions, into a pAAV backbone, between the human *Myo15a* promotor
496 and a non-oncogenic variant of WPRE (Zanta-Boussif *et al*, 2009) and the bovine growth
497 hormone derived poly-adenylation signal. Sequence integrity was confirmed by Sanger
498 sequencing. This vector was amplified in recombinase deficient *E. coli* NEB Stable (NEB) and
499 purified using the NucleoBond PC 2000 EF Mega kit for endotoxin free plasmid DNA
500 (Macherey-Nagel) according to the manufacturer's instructions.
501 Viral vector purification was performed essentially as previously published (Keppeler *et al*,
502 2018) and an extensive description is available in (Huet & Rankovic, 2021). In brief, triple
503 transfection of HEK-293T cells was performed using the pHelper plasmid (TaKaRa, USA),
504 trans-plasmid with the AAV-S capsid (Ivanchenko *et al*, 2021) and cis-plasmid with *YFP-*
505 *Palm3* under the control of the human *Myo15a* promotor. Cells were regularly tested for
506 mycoplasma contamination. Viral particles were harvested 72 hours after transfection from
507 the medium and 120 h after transfection from cells and the medium. Viral particles from
508 medium were precipitated with 40% polyethylene glycol 8000 (Acros Organics, Germany) in
509 500 mM NaCl for 2 h at 4 °C and then after centrifugation combined with cell pellets for
510 processing. Pellets were suspended in 500 mM NaCl, 40 mM Tris, 2.5 mM MgCl2, pH 8, and
511 100 U/ml of salt-activated nuclease (Arcticzymes, USA) at 37 °C for 2h (cells) or 30 min
512 (medium). Afterward, lysates were clarified by centrifugation at 2000 ×g for 10 min and viral
513 vectors were purified over iodixanol (Optiprep, Axis Shield, Norway) step gradients (15%,
514 25%, 40%, and 60%) at 350,000 × g for 2.25 h. Viral vectors were concentrated using Amicon
515 filters (EMD, UFC910024) and formulated in sterile phosphate-buffered saline (PBS)
516 supplemented with 0.001% Pluronic F-68 (Gibco, Germany). Viral vector titer was determined
517 by the number of DNase I resistant vg using AAV titration kit (TaKaRa/Clontech) with
518 adaptations to usage in crystal digital PCR (dPCR). Briefly, dilutions of purified DNA were

519 subjected to crystal dPCR using 5x Naica PCR reaction mix (Stilla, R10056) supplemented
520 with primers provided in the AAV titration kit, 0.8 mg/µl Alexa 647 (Invitrogen, 11570266) and
521 1.5x Eva Green (VWR, 31077-T). Formation of droplet crystals and PCR was performed in a
522 Naica Geode (Stilla) using Naica Ruby or Sapphire Chips (Stilla) and finally analyzed in the
523 Naica Prism3 reader (Stilla) equipped with Crystal Reader and Crystal Miner softwares (Stilla).
524 Purity of produced viruses was checked by silver staining (Pierce, Germany) after gel
525 electrophoresis (Novex™ 4–12% Tris–Glycine, Thermo Fisher Scientific) according to the
526 manufacturer's instruction. Viral stocks were kept at −80°C until usage.
527

528 **Postnatal AAV-Injection**

529 As systemic analgesia, *Palm3*$^{-/-}$ pups received subcutaneous injections of Buprenorphine
530 (0.1 mg/kg) and Carprofen (5 mg/kg) 30 min prior to the AAV-injection procedure. During the
531 procedure, anesthesia was induced with 5% isoflurane and maintained at 3% isoflurane. *AAV-*
532 S.*YFP-Palm3* was injected into the left ear via the round window method (Jung *et al*, 2015) at
533 postnatal day 4-6. Hearing assessment (ABR and DPOAE measurements) and cochlear
534 morphology were assessed 4-5 weeks post-injection. The virus solution was injected in a
535 concentration of 2.66×10^{12} genome copies/ml. All virus injection experiments were performed
536 in compliance with the national animal care guidelines and were approved by both the board
537 for animal welfare of the University Medical Center Göttingen and the State Animal Welfare
538 office of Lower Saxony (AZ19/3133).
539

540 **Confocal and STED microscopy**

541 Confocal imaging was performed using either a Leica SP8 microscope (Leica Microsystems,
542 Wetzlar Germany) or an Olympus-IX83 based Abberior Instruments Expert Line 775 nm 2-
543 color STED microscope (Abberior Instruments GmbH), operated in confocal mode. 2D-STED
544 images were acquired on a Nikon Eclipse Ti2-E based (Nikon, Tokyo, Japan) STEDYCON
545 system (Abberior Instruments GmbH) with a pulsed 775 nm depletion laser. Lasers with

546 wavelengths of 488, 587, and 633 nm were used for excitation. All 2D-STED images were
547 acquired using a 100x oil immersion objective (1.45 NA), with a final resolution of 54-56 nm.
548
549 **Prestin average fluorescence intensity**
550 Prestin average intensity analysis was performed by generating a mask of OHCs using the
551 *surfaces* algorithm in *Imaris* 10.2.0. For non-transduced OHCs, 3D reconstructions of Prestin
552 immunofluorescence were generated (surface detail: 0.15 µm, largest sphere diameter:
553 0.6 µm). For YFP-Palm3-transduced OHCs, YFP-Palm3 immunofluorescence signal was
554 rendered (surface detail: 0.163 µm, largest sphere diameter: 0.611 µm). Prestin average
555 intensity values from YFP-Palm3-transduced OHCs were normalized to values from non-
556 transduced controls. Prestin coefficient of variation analysis was performed using the
557 ImageJ/Fiji. Maximum projections were background-corrected by subtracting intensity
558 measured in a 3 µm x 3 µm area lacking apparent fluorescence intensity. Mean and standard
559 deviation were calculated from a 3 µm x 3 µm region within an OHC in the Prestin fluorescence
560 channel by plotting a histogram. The coefficient of variation was determined by dividing the
561 standard deviation by the mean.
562
563 **Statistics**
564 Statistical analyses were conducted using Prism 10 (GraphPad Software Inc, La Jolla, CA).
565 Normality of the data distribution was assessed with Kolmogorov-Smirnov normality test. For
566 comparisons between two groups, the two-tailed Wilcoxon matched-pairs signed-rank test
567 was used for paired data (e.g., IHC rescue cell count), and the two-tailed Mann-Whitney test
568 for unpaired, non-normally distributed data (e.g., spectrin intensity in WT vs *Palm3*-KO).
569 Unpaired multiple group comparisons (e.g., OHC degeneration along the tonotopic axis), were
570 analyzed with two-way ANOVA and Holm-Šídák's correction. For paired multiple comparisons
571 (e.g., rescue experiments), two-way repeated measures ANOVA with Holm-Šídák's correction
572 was applied. Single value plots display individual data points with mean ± standard error of
573 the mean (SEM). In violin plots, medians are indicated by solid lines and quartiles with dashed

lines. *N* indicates the number of animals, while *n* indicates the number of ears or hair cells, as specified accordingly in figure legends. Statistical significance is indicated by the symbols *n.s.* for not significant, $*P < 0.05$, $**P < 0.01$, $***P < 0.001$, and $****P < 0.0001$. A comprehensive summary table with all statistical information can be found in the Supplement of this article (**Supplemental Tables 1-3**).

580 # Results

581 ## Genetic deletion of *Palm3* results in severe, early onset and progressive
582 hearing loss in mice

583 To expand the initial findings of the GMC phenotypic screen, we extended the analysis window
584 for the auditory brainstem response (ABR) and distortion product otoacoustic emission
585 (DPOAE) measurements to juvenile (3-week-old) and young-adult (12-13-week-old) *Palm3*-
586 KO mice, along with their respective age-matched controls. We found an age-dependent
587 reduction in ABR Wave I (**Figure 1A-A'**). ABR thresholds to pure tone and click stimulation
588 were statistically significantly increased by 15-30 dB in juvenile *Palm3*-KO mice and then
589 further deteriorated in the older age group, where thresholds were elevated by 68 dB for clicks
590 and mostly exceeded our loudspeaker limit of 80 dB SPL for tone bursts (**Figure 1B-B'**). To
591 additionally evaluate OHC-mediated active cochlear amplification, distortion-product
592 otoacoustic emissions (DPOAEs) were recorded and found to already be markedly diminished
593 within the young age group (**Figure 1C-C'**), with a progressive decline leading to near-
594 complete loss of DPOAEs by 12-13 weeks of age (**Figure 1D-D'**). This latter finding is strongly
595 indicative of corrupted OHC function or cell loss.

596

597

598 ## In the murine cochlea, Palm3 is specifically and exclusively expressed in
599 auditory hair cells

600 To determine the expression of Palm3 within the peripheral auditory system, we conducted
601 immunohistochemical stainings on acutely dissected organs of Corti from post-hearing onset
602 wildtype mice. Samples were labeled using antibodies against Palm3, the cytosolic hair cell
603 marker Myosin7a, and the neuronal soma marker HuD (**Figure 1F**). In these experiments,
604 Palm3 localized specifically and exclusively to the lateral plasma membrane of both OHCs
605 and IHCs (**Figure 1G-H'**). To verify target specificity, we employed three independent

606 antibodies raised and affinity-purified against two distinct, non-overlapping and Palm3-specific
607 immunogen sequences: P31 and P32 (see Methods). All three antibodies produced identical
608 staining patterns, labeling only the lateral plasma membranes of both OHCs and IHCs, with
609 no detectable signals in other cell types within the sensory epithelium or the spiral ganglion
610 and a complete loss of staining in *Palm3*-KO preparations (**Supplementary figure 1**). This
611 cell-type specific expression aligns well with the publicly available single-cell RNA sequencing
612 data of auditory hair cells deposited on gEAR (**Supplementary figure 3**; Orvis *et al*, 2021;
613 https://umgear.org/). Palm3 was also detected in the lateral membranes of hair cells within the
614 vestibular system – including the macular organs and *cristae ampullaris* (**Supplementary**
615 **figure 4**).
616

617 **Hearing loss in *Palm3*-KOs results from progressive hair cell**
618 **degeneration**

619 Given the hearing deficits observed in *Palm3*-KO mice, which point toward dysfunction within
620 the peripheral auditory pathway, and the specific localization of Palm3 to the lateral plasma
621 membranes of IHCs and OHCs, we sought to elucidate the underlying mechanism by first
622 assessing the fate of IHCs and OHCs in the apical cochlear turn of *Palm3*-KO mice over a
623 time course from 2 to 50 weeks of age. Using Myosin7a as a marker for hair cells and the
624 DNA marker ToPro3 to label all nuclei for structural context, we found a pronounced and
625 progressive loss of OHCs starting as early as 2 weeks of age, with degeneration worsening
626 up to 50 weeks of age, where OHCs were almost completely lost (**Figure 2A-B**). These results
627 are consistent with the severely reduced DPOAE amplitudes in *Palm3*-KO mice (**Figure 1C-**
628 **D'**). Additionally, a mild but statistically significant loss of IHCs was observed (**Figure 2B**).
629 Notably, regardless of the specific subpopulation, remaining *Palm3*-KO hair cells displayed a
630 more compact and aberrant morphology in comparison to their age-matched WT counterparts
631 (**Figure 3A, B, C, C'**).
632

633 To test for tonotopic differences, we acquired *in situ* cytocochleograms to examine
634 frequency-specific OHC degeneration in *Palm3*-KO mice, using a modified iDisco protocol
635 (Keppeler *et al*, 2018). Here, cochleae of 2-week-old WT and *Palm3*-KO littermates were
636 chemically-cleared and immunostained with the hair cell marker Myosin7a. Then, we
637 employed lightsheet fluorescence microscopy to enable a detailed 3D analysis of hair cell
638 counts across the entire cochlear spiral. Myosin7a labeling served both to identify areas of
639 interest and to establish reference points for frequency band assignment (Müller *et al*, 2005;
640 Rankovic *et al*, 2021). Quantification of OHC survival was based on counts of Myosin7a-
641 positive OHCs within the computed frequency bands. Compared to age-matched WT controls,
642 *Palm3*-KO mice exhibited a significant reduction in OHC numbers across all three rows; yet,
643 with varying degrees (**Supplementary figure 5B-D**). The most extensive OHC loss occurred
644 in the 8-12 kHz band, where survival dropped by >50% across all rows. These results indicate
645 that loss of *Palm3* severely impacts cochlear function and OHC maintenance, warranting
646 further investigation into the mechanisms underlying these defects.
647
648

649 Genetic loss of *Palm3* results in reduced OHC length and perturbed 650 Prestin distribution within the OHC plasma membrane

651 Having observed that OHCs appeared abnormally 'compact' in *Palm3*-KOs, we further
652 investigated their morphology by measuring the lengths of OHCs in both pre-hearing (P11)
653 and hearing (P21) animals to assess the developmental onset, timing and severity of the
654 structural disturbance. Compared to WT controls, OHC length in P11 *Palm3*-KO mice was
655 reduced by ~22% (**Figure 3A,C**). This defect worsened in P21 *Palm3*-KO mice, with OHC
656 length reduced by ~40% (**Figure 3B,C'**). Even in heterozygous, *Palm3*-haploinsufficient
657 animals (8 weeks old), we observed a ~20% reduction in OHC length (**Supplementary figure
658 6**), which emphasizes the critical role of adequate Palm3 membrane levels in maintaining OHC
659 shape.

660

661 Noting the similarities between the *Palm3* mutant phenotype – particularly the
662 reduction in OHC length – and the known localization and knockout phenotype of Prestin
663 (Liberman *et al*, 2002; Zheng *et al*, 2000), we conducted additional IF analyses, which
664 confirmed the colocalization of Palm3 and Prestin within the OHC lateral plasma membrane
665 in wildtype mice (**Supplementary figure 7**). In *Palm3*-KO OHCs, the typical homogeneous
666 distribution of Prestin within the lateral plasma membrane was strikingly disrupted, exhibiting
667 fragmentation, heterogeneity, and partial internalization (**Figure 3A-B**). To further assess the
668 functional state of Prestin, we performed electrophysiological recordings on OHCs. Consistent
669 with the observed aberrant cell lengths, we found a significant reduction in the linear
670 capacitance (C_{lin}) of *Palm3*-KO OHCs, indicative of a reduced membrane surface area (**Figure**
671 **3E**). Non-linear capacitance (NLC), an electrophysiological proxy of Prestin function, remained
672 comparable to WT at P12-13, but declined at P18-20 in *Palm3*-KO OHCs (**Figure 3F**),
673 suggesting that progressive structural deterioration leads to reduced or mislocalized Prestin.
674 At P12-13, *Palm3*-KO OHCs displayed an elevated NLC to C_{lin} ratio (NLC/C_{lin}) (**Figure 3G**),
675 indicating elevated Prestin activity per unit membrane area, likely due to normal Prestin
676 production being confined into a progressively limited membrane space. By P18-20, NLC/C_{lin}
677 no longer differed from WT, indicating that Prestin packing density had reached saturation
678 despite fragmentation. Importantly, the voltage at peak capacitance (V_h) remained consistent
679 across all conditions, suggesting that the functional properties of Prestin were not significantly
680 altered (**Figure 3H**). However, the slope of the bell-shaped curve (**Figure 3D,D'**) showed a
681 significant decrease in *Palm3*-KO OHCs at P18-20, but not at P12-13 (**Figure 3I**), pointing to
682 the possibility that Prestin activity may be slightly altered.

683

684

685 **Palm3 precedes Prestin arrival in the OHC lateral membrane**

686 To investigate the developmental time course of membrane insertion for both Palm3 and
687 Prestin, we performed IF analyses on apical turns of whole-mount organ of Corti preparations
688 from various early postnatal stages up to the onset of hearing in mice (P0-P14,
689 **Supplementary figure 8A**). Simultaneous co-staining for Palm3 and Prestin within the same
690 organ of Corti was not feasible, as both antibodies were produced in rabbit. Instead, we
691 analyzed contralateral ears of the same animals to ensure comparability of staining. In these
692 experiments, αII-Spectrin was used as a common context marker in both preparations to
693 provide a spatial reference and allow for direct comparison of Palm3 and Prestin temporal
694 expression patterns. Palm3 labeling was prominently detectable in OHC lateral membranes
695 as early as P0, with labeling intensity increasing by P3 and stabilizing through P7, ultimately
696 reaching its peak intensity within the timeframe of this analysis at P14, indicating an early
697 developmental role (**Supplementary figure 8A,C**). In contrast, Prestin labeling emerged
698 around P3, consistent with previous studies (Oliver & Fakler, 1999; Legendre *et al*, 2008), and
699 progressively intensified, eventually reaching its highest observed level at P14 – aligning with
700 the maturation of OHC functionality. These findings reveal distinct temporal expression
701 patterns between Palm3 and Prestin, with Palm3 appearing earlier in development and
702 potentially contributing to membrane stabilization or organization required for adequate
703 Prestin localization.

704

705

706 **Palm3 affects spectrin isoform expression in the OHC submembrane**
707 **cytoskeleton**

708 Based on previous research highlighting the role of paralemmins in membrane-cytoskeleton
709 interactions (Kutzleb *et al*, 1998; Arstikaitis *et al*, 2008; Kutzleb *et al*, 2006; Nie *et al*, 2017;
710 Sáinz-Jaspeado *et al*, 2021) and the evident subcellular localization of Palm3 in the plasma
711 membrane compartment, we asked whether the recently described interaction of Palm1 with

712 βII-Spectrin in the periodic submembrane cytoskeleton of neuronal axons (Macarrón-Palacios
713 *et al*, 2025) could – by analogy – reflect a conserved paralemmin/spectrin association across
714 isoforms. First, we identified the most likely candidate spectrin isoforms by utilizing the publicly
715 available transcriptome profiling data for OHCs from the gEAR database (**Supplementary**
716 **figure 9**; Orvis *et al*, 2021; https://umgear.org/), revealing αII-, βI- and βII-Spectrin, but not αI-
717 , βIV- and βV-Spectrin to be detected in hair cells. These three isoforms were therefore
718 selected for further validation by immunohistochemistry and confocal microscopy. The co-
719 labelings with Palm3 confirmed that αII-, βI- and βII-Spectrin indeed co-localize with Palm3 at
720 the lateral walls of auditory hair cells (**Figure 4A-C'**). Additionally, all three spectrin isoforms
721 are found to be enriched in the actin-rich cuticular plates. Strikingly βI-Spectrin – a major
722 component of the erythrocytic membrane cytoskeleton – was robustly localized to the lateral
723 plasma membranes of IHCs and OHCs (**Figure 4B-B'**), with erythrocytes in blood vessels of
724 the organ of Corti serving as an internal positive control for target specificity (**Supplementary**
725 **figure 10**).
726
727 We next assessed whether Palm3 deficiency alters the abundance of individual
728 spectrins by measuring fluorescence intensities in the lateral wall of *Palm3*-KO OHCs. We
729 found that the average fluorescence intensity of αII-Spectrin was reduced by ~42% in *Palm3*-
730 KO OHC lateral membranes (**Figure 4G**), while βI-Spectrin exhibited a dramatic ~80%
731 decrease, indicating a strong Palm3 dependency for its stability and/or correct localization
732 (**Figure 4G'**). Lastly, in line with previous work (Liu *et al*, 2019) βII-Spectrin, which generally
733 showed the weakest signal intensity in the lateral membrane but is enriched in the cuticular
734 plates, declined by ~20% in fluorescence intensity (**Figure 4G"**). In contrast to our
735 observations at the lateral membranes, average fluorescence intensities in the cuticular plates
736 showed largely opposing trends: while αII-Spectrin and βI-Spectrin intensity increased by
737 ~49% and ~15% in absence of Palm3 respectively, βII-Spectrin declined by ~16%
738 (**Supplementary figure 11C**). These reciprocal shifts imply that *Palm3* deletion differentially

739 affects the targeting to or stabilization within the submembraneous cytoskeleton, thus leading
740 to compensatory re-distribution of spectrin isoforms between different compartments.
741
742 To define the relationship between Palm3 and these three spectrin isoforms within the
743 organ of Corti at higher spatial resolution, we used two-color 2D stimulated emission-depletion
744 (2D-STED) optical nanoscopy on whole-mount preparations of the organ of Corti. In these
745 experiments, samples were co-labeled with antibodies against Palm3 and each of the spectrin
746 isoforms – αII-, βI-, or βII-Spectrin – then embedded in melamine and sectioned into ~80-90
747 nm ultrathin slices (Revelo *et al*, 2014). This approach physically minimizes the third
748 dimension of the sample, and hence allowed us to capitalize on the maximum lateral resolution
749 of 2D-STED that would not be achievable in intact preparations due to tissue-based spherical
750 aberrations. This revealed unique staining patterns for Palm3 and the various spectrin
751 isoforms: Palm3 signal showed a striking punctate distribution along the OHC membrane
752 (**Figure 5A'-C'**), while αII-Spectrin and βI-Spectrin exhibited similar, yet somewhat more
753 continuous, staining patterns along the OHC membrane (**Figure 5A',B'**). In contrast, βII-
754 Spectrin displayed a broader labelling distribution, detected in both the OHC plasma
755 membrane and cytosol, but was mainly concentrated within the cuticular plates (**Figure**
756 **5C,C'**). Interestingly, while all spectrin staining patterns closely aligned with Palm3 along the
757 longitudinal as well as circumferential plasma membrane, βI-Spectrin in particular appeared
758 to closely follow the longitudinal staining pattern of Palm3 (**Figure 5A"'-C"'**). Notably,
759 compared to Palm3 IF, the spectrin IF distribution appeared slightly shifted towards the
760 intracellular space (**Figure 5A"-C"**).
761 To quantify the spatial relationship between Palm3 and each respective spectrin
762 isoform, we calculated Li's intensity correlation quotient (ICQ), which tests the correlation
763 between individual pixel intensities of two distinct staining patterns (Li *et al*, 2004). The
764 resulting ICQ value falls within a range of -0.5 and +0.5, where positive values indicate the
765 degree of colocalization or dependency, values near zero suggest random distribution, and
766 negative values imply segregation or mutual exclusion. ICQ analyses revealed positive ICQ

767 values for Palm3 and all tested spectrins, indicating a significant degree of staining
768 dependency between these proteins – in particular with αII- and βI-Spectrin (**Figure 5D-F**).
769
770

771 Palm3 appears periodically spaced in the OHC plasma membrane

772 Next, to obtain a better understanding of the Palm3 cluster distribution within the nano-
773 architecture of the OHC lateral membrane, we analyzed the nearest-neighbor distances
774 (NND) of Palm3 immunofluorescence puncta in our 2D-STED images. In longitudinally-
775 sectioned OHCs, the average Palm3 NND was 143 ± 1.5 nm, whereas in cross-sectioned
776 OHCs, representing circumferential distribution, the average NND was slightly shorter at 132
777 ± 1.5 nm ($N_{animals}$= 4; n_{images}= 6; n_{Palm3}= 953 for longitudinal; $N_{animals}$= 4; n_{images}= 8; n_{Palm3}= 891
778 for cross section). In a few cells, where the OHC plasma membrane was sectioned slightly
779 angled to enable an *en face* view (**Figure 6A,A'**), we could extend this analysis to measure
780 the NNDs of up to five of the closest surrounding Palm3 clusters (1st NND = 124 ± 0.8 nm, 3rd
781 NND = 161 ± 0.9 nm, 5th NND = 194 ± 1.1 nm; **Figure 6B**). Similarly, we could perform the
782 same type of analysis with αII-Spectrin (1st NND = 138 ± 2.4 nm, 3rd NND = 188 ± 2.4 nm, 5th
783 NND = 229 ± 2.6 nm; **Figure 6C**) and found that the observed distances are well within the
784 range of β-Spectrin spacing in neuronal axons – where spectrin IF exhibits a characteristic
785 periodicity pattern at ∽180-190 nm (Pan *et al*, 2018; Han *et al*, 2017; D'Este *et al*, 2015).
786 Collectively, these findings strongly indicate that (i) Palm3 co-localizes with the
787 submembraneous actin/spectrin cytoskeleton, where it – based on ICQ analysis – (ii) exerts
788 interdependency in particular with αII- and βI-Spectrins and (iii) appears to be evenly spaced
789 along the OHC circumference – albeit with a mild longitudinal stretch. Hence, these findings
790 further support the hypothesized molecular association between Palm3 and spectrin isoforms.
791
792

Loss of Palm3 disrupts the structure of the subsurface cisternae underneath the cortical lattice

To examine potential ultrastructural alterations in the lateral membrane of *Palm3*-KO OHCs, we next employed electron tomography on high-pressure frozen, freeze-substituted (HPF/FS) apical turns of the organ of Corti (Chakrabarti *et al*, 2018, 2022). This method enables high-resolution imaging while preserving near-native structural integrity, rendering it well-suited to compare the lateral wall ultrastructure of WT and *Palm3*-KO OHCs (**Figure 7A-B"**). Indeed, the tomographic reconstructions of the supranuclear SSCs and proximal plasma membrane revealed striking differences between genotypes: apical OHCs in *Palm3*-KO mice exhibited a substantial decrease in supranuclear SSC abundance along the lateral wall (**Figure 7C**). The few residual SSCs in *Palm3*-KO OHCs were positioned more distant from the plasma membrane compared to those in WT OHCs (**Figure 7D**), suggesting disrupted spatial arrangement – potentially due to impaired SSC anchoring within the lateral wall complex. Morphometric analysis also showed that SSCs in *Palm3*-KO OHCs appeared more flattened and structurally simplified, as indicated by reduced surface-to-volume ratios (**Figure 7E**). Beyond the SSC, mitochondria – which typically located proximal to the plasma membrane – were found at greater distances in *Palm3*-KO OHCs. This was confirmed by quantitative analysis, which showed a significant increase in the average distance between mitochondria and the plasma membrane (**Figure 7F**).

AAV-mediated *Palm3*-rescue partially restores hearing loss in *Palm3*-KO mice

Given that hair cell degeneration in *Palm3*-KO mice begins around the onset of hearing and progresses over time, we evaluated whether early postnatal viral rescue could prevent the pathophysiological consequences of *Palm3* loss. We used an adeno-associated viral vector (AAV.S; Ivanchenko *et al*, 2021) carrying a YFP-tagged *Palm3* fusion gene under the control

820 of the human *Myo15a* promoter (*AAV-S_Myo15a_YFP-Palm3*; **Figure 8A**; **Supplementary**
821 **figure 12**). The vector was delivered via unilateral intracochlear injection through the round
822 window membrane of *Palm3*-KO mouse pups at P4-6 (Rankovic *et al*, 2021). This method
823 enabled within-subject comparisons between injected (ipsilateral) and non-injected
824 (contralateral) ears to assess the functional and morphological magnitude of rescue efficacy.
825 Auditory function and cochlear morphology were then evaluated 4-5 weeks post-injection
826 (**Figure 8B**): *Palm3*-rescue mice exhibited modest hearing improvements (**Figure 8C-E**).
827 Specifically, ABR amplitudes in response to 100 dB and 20 Hz click stimulation as well as
828 pure-tone thresholds were mildly but statistically significantly improved in the injected ears
829 (**Figure 8C-D**). DPOAEs at the f2 frequency of 11.3 kHz show a trend towards increased
830 amplitudes in the injected ears, although this effect did not reach statistical significance
831 (**Figure 8E**).
832
833

834 OHC structure and survival rate are partially restored in AAV-rescued 835 *Palm3*-KO mice

836 To evaluate the structural and cellular effects of AAV-mediated *Palm3* rescue, cochleae were
837 collected post-ABR recordings and processed for subsequent IF analysis (**Figure 8F**). We
838 observed notable variability in OHC transduction efficiency, while IHCs consistently exhibited
839 higher transduction and expression rates (**Supplementary figure 13A**). This heterogeneity –
840 together with lack of target cell specificity – is probably responsible for the modest rescue
841 success at the systems level (ABR).
842 To determine whether viral *Palm3* re-introduction enhanced hair cell survival in *Palm3*-
843 KO mice, we quantified hair cells within a defined 300 x 300 µm region of the apical cochlear
844 turn of the organ of Corti in *Palm3*-rescue animals. IHC counts showed a slight reduction of
845 ~11.6% in the ipsilateral ear (**Supplementary figure 13B**) which is more pronounced than
846 the weak impact of the *Palm3*-KO itself at 7-8 weeks (~6%, WT: 25.0 ± 1.16; *Palm3*-KO: 23.5

847 ± 0.22; **Figure 2B**) – presumably due to cytotoxic effects from aberrant Palm3 expression or
848 to viral (over-) load, which appear to disrupt IHC morphology and compromise cellular
849 structural homeostasis (**Supplementary figure 13C**). In contrast, in OHCs which are severely
850 affected by the *Palm3*-KO, a beneficial effect of the rescue prevailed: OHC survival in the
851 ipsilateral ears trended upwards, particularly in the innermost (OHC1, ~53%) and middle rows
852 (OHC2, ~41%) (**Figure 8H**).

853 To assess whether the structural integrity of OHCs was restored in *Palm3*-transduced
854 cells, we further examined cellular length. Transduced OHCs displayed elongated and
855 creased plasma membranes, resembling the wildtype morphology (**Figure 8G**). Quantitative
856 assessment of OHC length confirmed length restoration in ipsilateral ears, reaching values
857 comparable to OHCs in P21 WT mice (**Figure 8I**; **Figure 3C'**). Together, these results suggest
858 that AAV-mediated *Palm3* delivery in *Palm3*-KO mice generally supports improved OHC
859 survival and facilitates structural restoration, thus resulting in the functional improvements
860 observed in **Figure 8C-E**.

861

862

863 Viral Palm3 rescue reestablishes αII-Spectrin and Prestin abundance in 864 *Palm3*-KO OHCs

865 To further assess the cellular effects of *Palm3* rescue on the plasma membrane scaffold of
866 *Palm3*-KO OHCs, we examined whether the expression of αII-Spectrin could be restored. As
867 αII-Spectrin heterodimerizes with βI- as well as βII-Spectrins, it served as a surrogate to
868 assess spectrin scaffold integrity. Quantitative IF analysis revealed a statistically significant
869 increase in αII-Spectrin average fluorescence intensity in *Palm3*-transduced OHCs compared
870 to neighboring non-transduced OHCs within the same organ of Corti (**Figure 8J,J'**). These
871 results suggest that *Palm3* re-introduction restores αII-Spectrin expression in the lateral
872 membrane.

873 Finally, we investigated whether *Palm3* rescue would also restore the irregular and
874 clustered distribution of Prestin in *Palm3*-KO OHCs (**Figure 3B**). Indeed, Prestin staining
875 appeared visually more homogeneous relative to that in non-transduced OHCs (**Figure 8K**).
876 Quantitative analysis revealed a slight decrease in average Prestin fluorescence intensity in
877 *Palm3*-transduced OHCs, likely due to the loss of abnormally high-intensity IF signal clusters
878 and a transition toward a more homogeneous distribution as observed in wildtype OHCs
879 (**Figure 8K'**). Supporting this, the coefficient of variation (CV) of Prestin IF puncta intensity
880 was significantly higher in *Palm3*-KO than in *Palm3*-recued OHCs, indicating greater spatial
881 heterogeneity in Prestin distribution in the KOs (**Figure 8K"**). Conversely, the lower CV
882 observed in *Palm3*-transduced OHCs suggests a restoration of a more uniform Prestin
883 distribution along the lateral membrane.
884
885

886 ## Discussion

887 In the present study, we investigated the functional and morphological consequences of
888 *Palm3* deficiency within the peripheral auditory system. Alongside systems-physiological
889 analyses, we employed immunohistochemistry in combination with a range of advanced
890 microscopy techniques – including lightsheet fluorescence microscopy, confocal and 2D-
891 STED microscopy, as well as electron tomography – to elucidate the consequences of *Palm3*
892 loss on the morphology and function of OHCs. Our findings reveal that *Palm3*-deficient mice
893 exhibit early-onset, progressive hearing loss that was associated with gradual degeneration
894 of auditory hair cells along the entire tonotopic axis of the cochlea. Palm3 localizes specifically
895 to the lateral plasma membranes of IHCs and OHCs, where it stabilizes the cortical lattice. In
896 OHCs, in particular, the absence of *Palm3* leads to cell length reduction, disrupted distribution
897 of Prestin, misdistribution of spectrins, and a decrease in the number and structural integrity
898 of subsurface cisternae (SSCs) along the OHC lateral plasma membrane. AAV-mediated
899 rescue of *Palm3*-KO animals partially restored auditory function, due to enhanced OHC

900 survival and restoration of OHC lengths, and re-establishment of αII-Spectrin expression and
901 proper Prestin localization. Together, these findings highlight a critical role for Palm3 in
902 maintaining the structural integrity and function of auditory hair cells and demonstrate its
903 potential as a novel deafness gene.
904
905

906 Genetic loss of *Palm3* disrupts cochlear amplification and OHC 907 integrity by compromising cytoskeletal and membrane stability

908 Genetic loss of Palm3 leads to a substantial ~50 dB SPL elevation in auditory thresholds and
909 a near-complete loss of active cochlear amplification, indicating its critical role in peripheral
910 auditory processing. Localized to the lateral plasma membrane of auditory hair cells, Palm3
911 is essential for maintaining hair cell integrity – particularly in OHCs. This heightened
912 dependency of OHCs on Palm3 is likely due to their specialized role in voltage-driven somatic
913 electromotility and the concomitant demand on the stability of their lateral cell wall (Borkó *et*
914 *al*, 2005; Batta *et al*, 2003; Hallworth, 1995; He & Dallos, 2000).
915 The severe vulnerability of *Palm3*-KO OHCs is reminiscent of the phenotype observed
916 in *Palmd*-KO endothelial cells, where reduced mechanical resilience via disrupted nuclear
917 actin caps contributes to pathology (Sáinz-Jaspeado *et al*, 2021). Similarly, OHCs highly
918 depend on a well-organized actin/spectrin cytoskeleton to support both their somatic
919 electromotility and structural integrity (Brownell, 1990; Holley *et al*, 1992; Oghalai *et al*, 1998;
920 Holley & Ashmore, 1990; Wada *et al*, 2004). In *Palm3*-KO OHCs, mis-distribution of αII-, βI-
921 and βII-Spectrins from the lateral plasma membrane to the cuticular plate indicates
922 destabilization of the submembrane skeleton (Yao *et al*, 2022; Liu *et al*, 2019), while
923 abnormalities in SSCs and misplacement of membrane-proximal mitochondria indicate that
924 the disruption of the submembrane skeleton also perturbs the ultrastructural organization of
925 these endomembrane compartments (Lue & Brownell, 1999; Perkins *et al*, 2020) and possibly
926 OHC energetics (Song & Santos-Sacchi, 2015). While Prestin distribution is altered in *Palm3*-

927 KO OHCs, their NLC remains largely preserved in young pre-hearing mice, suggesting that
928 electromotility *per se* is not affected. Therefore, degeneration likely arises from compromised
929 mechanical resilience due to aberrant cytoskeletal and ultrastructural integrity that renders
930 OHCs vulnerable to recurrent membrane distortion. In contrast, IHCs – which do not engage
931 in somatic motility – exhibit milder structural defects, indicating a lesser reliance on these
932 same membrane characteristics (Ashmore, 2008; Peng & Ricci, 2011). Future studies – e.g.,
933 involving chronic sound deprivation or excessive noise during rearing – could clarify whether
934 mechanical stress is the principal driver of OHC degeneration.

935 Building on the observed cytoskeletal and lateral membrane disorganization in *Palm3*-
936 KO OHCs, we examined whether such structural abnormalities might also impact the
937 localization and functional stability of Prestin over time. The striking overlap in localization
938 patterns between Palm3 and Prestin, along with the similar reduction in OHC lengths observed
939 in both *Palm3*- and *Prestin*-KO mice, suggest a functional connection between the two
940 proteins. In *Palm3*-KO mice, Prestin becomes aberrantly distributed within the OHC lateral
941 membrane. Despite this mislocalization, NLC remains unaltered in younger animals, indicating
942 preserved voltage-dependent behavior and blanket distribution of Prestin at early
943 developmental stages. In contrast, the significant reduction in NLC observed in older *Palm3*-
944 KO mice suggests a progressive decline in electromotility. Such a decline has been previously
945 linked to Prestin-associated factors including direct functional impairment (Liberman *et al*,
946 2002; He *et al*, 2009; Dallos *et al*, 2008), altered protein expression (Cheatham *et al*, 2015;
947 Seymour *et al*, 2016; Abe *et al*, 2007), or disrupted membrane localization (Zheng *et al*, 2005;
948 Sturm *et al*, 2007). In our study, the fragmented and patchy distribution of Prestin within the
949 lateral membrane of *Palm3*-KO OHCs, which became increasingly pronounced with
950 advancing age, likely contributes to the observed disruption of NLC in the older animals.

951 Further analysis of NLC/C_{lin} ratio revealed elevated values in younger *Palm3*-KO
952 OHCs compared to WT, suggesting relatively higher Prestin activity per unit membrane area.
953 This likely reflects normal Prestin production while the membrane surface area decreases,
954 leading to greater protein packing density within the available membrane space. In older

955 *Palm3*-KO mice, the ratio resembled that of wildtype values, suggesting that Prestin had
956 reached its maximal packing density. Yet, despite the uneven membrane distribution of Prestin
957 observed in *Palm3*-KO OHCs, the overall Prestin levels appear comparable to those in WT
958 OHCs. Supporting this, V_h – a reliable indicator of Prestin functional maturation (Oliver &
959 Fakler, 1999; Santos-Sacchi & Tan, 2018) – remained stable across age groups and
960 genotypes, indicating that Prestin protein function as such is largely preserved in *Palm3*-KO
961 OHCs. Taken together, our findings indicate that while Palm3 is not essential for the core
962 function or expression of Prestin, it plays a critical role in maintaining proper membrane
963 organization and distribution of Prestin over time.
964
965

966 Palm3 contributes to the stability and maintenance of the OHC
967 submembrane cytoskeleton

968 Consistent with earlier work implicating other Paralemmin isoforms in membrane-cytoskeleton
969 dynamics (Kutzleb *et al*, 1998; Arstikaitis *et al*, 2008; Sáinz-Jaspeado *et al*, 2021; Macarrón-
970 Palacios *et al*, 2025), we observed that *Palm3* deletion leads to a significant reduction in the
971 lateral membrane localization of αII-, βI- and βII-Spectrins. These findings underscore the role
972 of Palm3 in maintaining submembrane cytoskeleton integrity within this specialized plasma
973 membrane domain. The varying degrees of signal loss across the investigated spectrin
974 isoforms further suggest differential regulatory mechanisms and potentially isoform-specific
975 interactions or dependencies for membrane recruitment and/or stabilization. Interestingly, we
976 found the effects of Palm3 loss to extend beyond the lateral wall. The reduced βII-Spectrin
977 intensity in the cuticular plate of *Palm3*-KO OHCs raises the possibility that Palm3 may
978 contribute to spectrin organization across distinct cytoskeletal compartments, potentially
979 through indirect mechanisms such as trafficking or scaffolding. In contrast, the observed
980 increase of αII- and βI-Spectrin in the cuticular plates of *Palm3*-KO OHCs may reflect a
981 compensatory response to impaired membrane anchoring within the lateral wall. Whether this

982 effect involves direct interaction with spectrins or is mediated through intermediary scaffolding
983 proteins remains to be clarified.
984 Using 2D-STED microscopy on ultrathin melamine-embedded sections, we observed
985 that Palm3 exhibits a membrane-associated spacing of ~124-194 nm in OHCs, with distances
986 slightly varying between longitudinal and circumferential orientations. This pattern falls within
987 the range reported for β-Spectrin periodicity and length in neurons and erythrocytes (Pan *et*
988 *al*, 2018; Zhong *et al*, 2014; Bennett *et al*, 1982; Shotton *et al*, 1979; D'Este *et al*, 2015, 2017),
989 raising the possibility that Palm3 aligns with spectrins to orchestrate the membrane-
990 cytoskeleton architecture. However, unlike the well-organized linear arrays seen in axons
991 (Macarrón-Palacios *et al*, 2025; D'Este *et al*, 2015), the OHC lateral wall is subject to dynamic
992 mechanical changes during electromotility, likely resulting in a more complex and flexible
993 cytoskeletal meshwork (Holley, 1996). This distinction may better resemble the three-
994 dimensional subcortical actin/spectrin meshwork found in erythrocytes, where structural
995 integrity is balanced with mechanical deformability. The slightly extended longitudinal spacing
996 of Palm3 (~143 nm) compared to its circumferential distribution (~132 nm) is consistent with
997 the observations in neuronal axons, where microtubular stretch regulates β-Spectrin
998 organization and supports its full-length extension (Zhong *et al*, 2014). In line with this
999 hypothesis, the longitudinal microtubule network of auditory hair cells is primarily oriented in
1000 an apico-basal direction (Steyger *et al*, 1989; Furness *et al*, 1990; Voorn *et al*, 2024), and
1001 would thus enable a greater longitudinal spacing of Palm3. Additionally, Palm3 exhibited
1002 enrichment peaks along the OHC circumference that overlapped with those of αII- and βI-
1003 Spectrin. Together with the positive ICQ values, this finding suggests tight colocalization within
1004 the same subcellular compartment and implies a functional dependency.
1005
1006

1007 Palm3 stabilizes the submembrane cytoskeleton to maintain SSC
1008 integrity

1009 As prominent structures of the OHC lateral wall (Dieler *et al*, 1991), SSCs have been proposed
1010 to support electromotility by modulating voltage signaling – either via electro-osmotic effects
1011 near the plasma membrane (Kachar *et al*, 1986) or by facilitating rapid transmission of
1012 membrane potential changes to Prestin-rich domains (Song & Santos-Sacchi, 2015).
1013 Moreover, SSCs facilitate vesicular trafficking (Kaneko *et al*, 2006) and likely serve as
1014 intracellular calcium reservoirs (Schulte, 1993). In *Palm3*-KO OHCs, SSCs were strikingly
1015 reduced in number and displayed a vastly simplified complexity, with the few remaining
1016 structures appearing flattened and displaced from the plasma membrane. On first sight, this
1017 suggests intrinsic structural collapse of SSCs; however, their distal positioning more likely
1018 reflects secondary consequences of cytoskeletal disruption, potentially due to impaired
1019 anchoring to the submembrane cytoskeleton in the absence of Palm3. Considering the
1020 reduced spectrin expression in *Palm3*-KO OHCs, this anchoring defect is more plausibly a
1021 result of a broader collapse of the submembrane cytoskeleton, rather than being a direct
1022 consequence of *Palm3* loss alone. Collectively, these results indicate that Palm3 plays a
1023 critical role in the maintenance of the SSCs, likely by contributing to the stability of the
1024 submembrane cytoskeleton. Interestingly, prior research on salicylate-induced SSC damage
1025 has linked SSC disruption to decreased stiffness of the lateral wall, leading to compromised
1026 OHC lateral wall mechanics and impaired electromotility (Lue & Brownell, 1999; Song &
1027 Santos-Sacchi, 2015; Shehata *et al*, 1991). Such functional deficits may underlie the near-
1028 complete loss of cochlear amplification observed at three weeks of age, even in the presence
1029 of surviving OHCs.
1030
1031
1032

1033 Palm3 as a component of the pillar complex?

1034 'Pillars' have been described as electron-dense, periodically-spaced structures that connect
1035 the OHC plasma membrane to the underlying submembrane cytoskeleton. Early

1036 ultrastructural studies reported pillars to average around ~30 nm in length (Holley & Ashmore,
1037 1990). Further investigations revealed that pillars likely behave as entropic springs, varying in
1038 length from 17 to 51 nm, with an average spacing of 26 ± 11 nm along actin filaments.
1039 Moreover, pillars were found to extend into a Y-shape as the distance between the OHC
1040 plasma membrane and the underlying cytoskeleton increases, and flatten against the
1041 membrane as that distance decreases (Forge, 1991; Holley *et al*, 1992; Triffo *et al*, 2019).
1042 Despite their discovery in the late 1980s, the molecular identity of these structures remains
1043 unresolved to date. We propose that Palm3 may serve as a key component of the pillar protein
1044 complexes. Several lines of evidence support this hypothesis: (i) Palm3 contains a CaaX motif,
1045 confirming its definitive localization to the plasma membrane. (ii) Pillar-like structures are
1046 present in both OHCs and IHCs (Furness & Hackney, 1990), which is consistent with Palm3
1047 expression in both cell types. (iii) Due to the overlapping localization pattern of
1048 Palm3/spectrins, the dramatic reduction of spectrins within the lateral wall of *Palm3*-KO OHCs
1049 and drawing from the analogy with Palm1 (i.e., assuming that spectrin-binding is conserved
1050 across paralemmins), Palm3 may similarly associate with spectrins, although direct evidence
1051 to substantiate this link remains to be established. (iv) Palm3 exhibits a seemingly periodic
1052 and clustered distribution that resembles the spectrin staining pattern in erythrocytes,
1053 suggesting a potential structural parallel in cytoskeletal organization, which however differs in
1054 the extent of spectrin extension. (vi) Finally, the flexible, entropic spring-like behavior of pillars
1055 is compatible with the predicted intrinsically-disordered nature of Palm3, which could allow
1056 Palm3 to accommodate dynamic changes in cytoskeletal architecture along the OHC lateral
1057 wall.

1058 However, certain discrepancies emerge when comparing the known dimensions and
1059 periodicity of pillars with our Palm3 data. Specifically, Palm3 puncta observed through 2D-
1060 STED NND and line profile-based peak-to-peak analyses show significantly wider spacing
1061 (~125-194 nm) than the reported EM-based spacing range of ~17-51 nm for individual pillars.
1062 This difference may stem from technical limitations of the immunofluorescence techniques,
1063 including reduced spatial accuracy due to bulky antibody-fluorophore conjugates and potential

1064 clustering artifacts induced by chemical fixation. Importantly, variations in sample preparation,
1065 particularly the use of distinct chemical fixation procedures must be considered, as they can
1066 introduce significant variability. Alternatively, it also remains a possibility that Palm3 is not part
1067 of the pillar complexes but instead contributes more broadly to lateral membrane stability,
1068 which is a possibility that warrants further exploration through high-resolution structural and
1069 biochemical approaches. In conclusion, our data suggests that Palm3 represents a formidable
1070 – and, to date, to our knowledge the *only* – protein candidate to contribute to pillar complexes
1071 since these structures were first described.
1072
1073

1074 Viral rescue at early postnatal stages can successfully correct *Palm3* 1075 loss from OHCs

1076 Given the early onset of OHC degeneration in *Palm3*-KO mice and recent associations
1077 between *Palm3* mutations and age-related hearing loss in humans (Cornejo-Sanchez *et al*,
1078 2025), our evaluation of AAV-mediated *Palm3* rescue reveals important insights into its
1079 potential for future therapeutic intervention. Since OHC degeneration in *Palm3*-KO mice
1080 begins around hearing onset, this period represents a critical early postnatal window of
1081 opportunity, during which gene therapy may effectively counteract the pathological
1082 consequence of *Palm3* loss. In line with this, our study shows that postnatal reintroduction of
1083 wildtype *Palm3* can alleviate the detrimental phenotype associated with its deficiency.
1084 Specifically, OHC survival was markedly improved compared to the pronounced degeneration
1085 seen in *Palm3*-KO mice by five weeks of age. In addition to enhanced survival, *Palm3*-rescued
1086 OHCs exhibited notable restoration in cell length, indicating a clear recovery toward normal
1087 cellular morphology. At the molecular level, *Palm3* reintroduction restored proper expression
1088 of αII-Spectrin and corrected the aberrant distribution of Prestin along the OHC lateral
1089 membrane. These findings demonstrate that postnatal re-introduction of *Palm3* effectively

1090 reverses the key deficits associated with its loss and further emphasize the essential role of
1091 Palm3 in stabilizing the lateral membrane and maintaining OHC structural integrity.
1092 However, despite the significant cellular and morphological improvements observed in
1093 *Palm3*-rescued OHCs, these structural restorations translated into only modest recovery of
1094 hearing function, pointing to several limitations that may have collectively constrained the
1095 therapeutic outcome: (i) The transduction efficiency was highly variable across rescue
1096 animals, with especially poor targeting of vulnerable OHCs and more consistent delivery to
1097 the less affected IHCs. (ii) Off-target effects due to the broad tropism of the AAV.S vector
1098 (Ivanchenko *et al*, 2021) – including *Palm3* overexpression in IHCs, stereociliar mislocalization
1099 that may exert a negative impact on mechanotransduction, and ectopic transduction of SGNs
1100 – likely compromised cellular structural homeostasis, introduced cellular stress, and impaired
1101 synaptic function to ultimately further compromise auditory function. Lastly, (iii) potential AAV-
1102 induced cytotoxicity (Meyers *et al*, 2001; Hirsch *et al*, 2011; Rapti *et al*, 2015; Johnston *et al*,
1103 2021), which has previously also been reported in the auditory system (Wei *et al*, 2025),
1104 cannot be excluded as a contributing factor to IHC loss. Future studies should aim for
1105 improved vector specificity, tightly controlled gene expression, and optimized delivery
1106 strategies to enhance *Palm3* gene therapy in future studies. Nevertheless, despite current
1107 limitations, this study provides a proof-of-concept which lays the groundwork for advancing
1108 the therapeutic potential of *Palm3*-based gene therapy.
1109

1110 Concluding remarks

1111 In summary, this study identifies Palm3 as a critical molecular component of the peripheral
1112 auditory system, that is essential for maintaining the structural integrity of the OHC lateral wall.
1113 Our findings introduce a promising novel deafness gene candidate and address a major gap
1114 in the molecular understanding of cochlear architecture – the molecular nature of the elusive
1115 pillar complexes between the plasma membrane and the cortical cytoskeleton.
1116

Acknowledgements

We would like to express our utmost gratitude to Christiane Senger-Freitag, Sandra Gerke and Jana Erlmoser for expert technical support, Nicole Metzendorf for initial AAV plasmid cloning and Rudolph Glückert for assistance with the ultrathin melamine-sectioning. This work was funded by a research grant from the Deutsche Forschungsgemeinschaft (DFG, German Research Foundation) – Project Number VO 2466/1-1 to CV and MWK, an *Otto Creutzfeldt Fellowship* of the Elisabeth and Helmuth Uhl Foundation (to CV), and intramural funding of the Medical University Innsbruck (to CV) and the CRC 889/3 project A07 to CW. The High-pressure-freezer was funded by the Deutsche Forschungsgemeinschaft (DFG, German Research Foundation) – Project number 257917528. The transmission electron microscope JEM1011 was funded by the Deutsche Forschungsgemeinschaft (DFG, German Research Foundation) – Project number 130725592. The transmission electron microscope JEM2100Plus was funded by REACT-EU from "Europäische Fonds für regionale Entwicklung (EFRE)" with the project *"ETomoH&H: Elektronentomografie an Herz und Hirn"* and the University Medical Center Göttingen.

Conflict of Interest

The authors declare no conflict of interest.

Author contributions

CV and MWK conceived the project and designed the experiments. VCH and CV performed immunohistochemistry, confocal imaging and data analysis. VCH performed STED immunohistochemistry, melamine sample embedding and STED imaging. VCH did chemical clearing and lightsheet microscopy. DD, MFK and DO performed OHC electrophysiology and analysis. GH performed cDNA sequencing, cloning and purification of Palm3 fusion proteins for immunisation, affinity-purification and pre-testing (Western blot) of sera. IB and NS measured and analyzed ABRs and DPOAEs. LS performed HPF/FS and TEM with assistance

1144 from VCH. CU and CW performed the electron tomography. KK designed and generated
1145 rescue AAVs. VCH, CV and MWK wrote the paper, VCH and CV generated all Figures. All co-
1146 authors revised the manuscript.

References

Abe T, Kakehata S, Kitani R, Maruya S, Navaratnam D, Santos-Sacchi J & Shinkawa H (2007) Developmental Expression of the Outer Hair Cell Motor Prestin in the Mouse. *J Membrane Biol* 215: 49–56

Arstikaitis P, Gauthier-Campbell C, Carolina Gutierrez Herrera R, Huang K, Levinson JN, Murphy TH, Kilimann MW, Sala C, Colicos MA & El-Husseini A (2008) Paralemmin-1, a Modulator of Filopodia Induction Is Required for Spine Maturation. *MBoC* 19: 2026–2038

Ashmore J (2008) Cochlear Outer Hair Cell Motility. *Physiological Reviews* 88: 173–210

Bannister LH, Dodson HC, Astbury AR & Douek EE (1988) Chapter 23 The cortical lattice: a highly ordered system of subsurface filaments in guinea pig cochlear outer hair cells. In *Progress in Brain Research* pp 213–219. Elsevier

Batta TJ, Panyi G, G□sp□r R & Sziklai I (2003) Active and passive behaviour in the regulation of stiffness of the lateral wall in outer hair cells of the guinea-pig. *Pfl□gers Archiv European Journal of Physiology* 447: 328–336

Bennett V, Davis J & Fowler WE (1982) Brain spectrin, a membrane-associated protein related in structure and function to erythrocyte spectrin. *Nature* 299: 126–131

Borkó R, Batta TJ & Sziklai I (2005) Slow motility, electromotility and lateral wall stiffness in the isolated outer hair cells. *Hearing Research* 207: 68–75

Brownell WE (1990) Outer Hair Cell Electromotility and Otoacoustic Emissions: *Ear and Hearing* 11: 82–92

Chakrabarti R, Jaime Tobón LM, Slitin L, Redondo Canales M, Hoch G, Slashcheva M, Fritsch E, Bodensiek K, Özçete ÖD, Gültas M, *et al* (2022) Optogenetics and electron tomography for structure-function analysis of cochlear ribbon synapses. *eLife* 11: e79494

Chakrabarti R, Michanski S & Wichmann C (2018) Vesicle sub-pool organization at inner hair cell ribbon synapses. *EMBO Reports* 19: e44937

Cheatham MA, Edge RM, Homma K, Leserman EL, Dallos P & Zheng J (2015) Prestin-Dependence of Outer Hair Cell Survival and Partial Rescue of Outer Hair Cell Loss in PrestinV499G/Y501H Knockin Mice. *PLoS ONE* 10: e0145428

Cornejo-Sanchez DM, Bharadwaj T, Dong R, Wang GT, Schrauwen I, DeWan AT & Leal SM (2025) Mendelian non-syndromic and syndromic hearing loss genes contribute to presbycusis. *Eur J Hum Genet*

Dallos P, Wu X, Cheatham MA, Gao J, Zheng J, Anderson CT, Jia S, Wang X, Cheng WHY, Sengupta S, *et al* (2008) Prestin-Based Outer Hair Cell Motility Is Necessary for Mammalian Cochlear Amplification. *Neuron* 58: 333–339

D'Este E, Kamin D, Balzarotti F & Hell SW (2017) Ultrastructural anatomy of nodes of Ranvier in the peripheral nervous system as revealed by STED microscopy. *Proc Natl Acad Sci USA* 114

1186 D'Este E, Kamin D, Göttfert F, El-Hady A & Hell SW (2015) STED Nanoscopy Reveals the
1187 Ubiquity of Subcortical Cytoskeleton Periodicity in Living Neurons. *Cell Reports* 10:
1188 1246–1251

1189 Dieler R, Shehata-Dieler WE & Brownell WE (1991) Concomitant salicylate-induced
1190 alterations of outer hair cell subsurface cisternae and electromotility. *J Neurocytol* 20:
1191 637–653

1192 Flock Å, Flock B & Ulfendahl M (1986) Mechanisms of movement in outer hair cells and a
1193 possible structural basis. *Arch Otorhinolaryngol* 243: 83–90

1194 Forge A (1991) Structural features of the lateral walls in mammalian cochlear outer hair cells.
1195 *Cell Tissue Res* 265: 473–483

1196 Forge A, Zajic G, Li L, Nevill G & Schacht J (1993) Structural variability of the sub-surface
1197 cisternae in intact, isolated outer hair cells shown by fluorescent labelling of
1198 intracellular membranes and freeze-fracture. *Hearing Research* 64: 175–183

1199 Fuchs PA, Lehar M & Hiel H (2014) Ultrastructure of cisternal synapses on outer hair cells of
1200 the mouse cochlea. *J Comp Neurol* 522: 717–729

1201 Furness DN & Hackney CM (1990) Comparative ultrastructure of subsurface cisternae in inner
1202 and outer hair cells of the guinea pig cochlea. *Eur Arch Otorhinolaryngol* 247

1203 Furness DN, Hackney CM & Steyger PS (1990) Organization of microtubules in cochlear hair
1204 cells. *J Elec Microsc Tech* 15: 261–279

1205 Greenwood DD (1961) Critical Bandwidth and the Frequency Coordinates of the Basilar
1206 Membrane. *The Journal of the Acoustical Society of America* 33: 1344–1356

1207 Gulley RL & Reese TS (1977) Regional specialization of the hair cell plasmalemma in the
1208 organ of corti. *Anat Rec* 189: 109–123

1209 Hallworth R (1995) Passive compliance and active force generation in the guinea pig outer
1210 hair cell. *Journal of Neurophysiology* 74: 2319–2328

1211 Han B, Zhou R, Xia C & Zhuang X (2017) Structural organization of the actin-spectrin–based
1212 membrane skeleton in dendrites and soma of neurons. *Proc Natl Acad Sci USA* 114

1213 He DZZ & Dallos P (2000) Properties of Voltage-Dependent Somatic Stiffness of Cochlear
1214 Outer Hair Cells. *JARO* 1: 64–81

1215 He DZZ, Jia S, Sato T, Zuo J, Andrade LR, Riordan GP & Kachar B (2009) Changes in plasma
1216 membrane structure and electromotile properties in prestin deficient outer hair cells.
1217 *Cytoskeleton*: n/a-n/a

1218 Hintze A, Lange F, Steyer AM, Anstatt J, Möbius W, Jakobs S & Wichmann C (2024)
1219 Developmental changes of the mitochondria in the murine anteroventral cochlear
1220 nucleus. *iScience* 27: 108700

1221 Hirsch ML, Fagan BM, Dumitru R, Bower JJ, Yadav S, Porteus MH, Pevny LH & Samulski RJ
1222 (2011) Viral Single-Strand DNA Induces p53-Dependent Apoptosis in Human
1223 Embryonic Stem Cells. *PLoS ONE* 6: e27520

1224 Holley MC (1996) Outer Hair Cell Motility. In *The Cochlea*, Dallos P Popper AN & Fay RR
1225 (eds) pp 386–434. New York, NY: Springer New York

1226 Holley MC & Ashmore JF (1988) A cytoskeletal spring in cochlear outer hair cells. *Nature* 335

1227 Holley MC & Ashmore JF (1990) Spectrin, actin and the structure of the cortical lattice in
1228 mammalian cochlear outer hair cells. *Journal of Cell Science* 96: 283–291

1229 Holley MC, Kalinec F & Kachar B (1992) Structure of the cortical cytoskeleton in mammalian
1230 outer hair cells. *Journal of Cell Science* 102: 569–580

1231 Huang G & Santos-Sacchi J (1993) Mapping the distribution of the outer hair cell motility
1232 voltage sensor by electrical amputation. *Biophysical Journal* 65: 2228–2236

1233 Huet AT & Rankovic V (2021) Application of Targeting-Optimized Chronos for Stimulation of
1234 the Auditory Pathway. In *Channelrhodopsin*, Dempski RE (ed) pp 261–285. New York,
1235 NY: Springer US

1236 Hultqvist G, Ocampo Daza D, Larhammar D & Kilimann MW (2012) Evolution of the Vertebrate
1237 Paralemmin Gene Family: Ancient Origin of Gene Duplicates Suggests Distinct
1238 Functions. *PLoS ONE* 7: e41850

1239 Ikeda K & Takasaka T (1993) Confocal laser microscopical images of calcium distribution and
1240 intracellular organelles in the outer hair cell isolated from the guinea pig cochlea.
1241 *Hearing Research* 66: 169–176

1242 Ivanchenko MV, Hanlon KS, Hathaway DM, Klein AJ, Peters CW, Li Y, Tamvakologos PI,
1243 Nammour J, Maguire CA & Corey DP (2021) AAV-S: A versatile capsid variant for
1244 transduction of mouse and primate inner ear. *Molecular Therapy - Methods & Clinical*
1245 *Development* 21: 382–398

1246 Jing Z, Rutherford MA, Takago H, Frank T, Fejtova A, Khimich D, Moser T & Strenzke N
1247 (2013) Disruption of the Presynaptic Cytomatrix Protein Bassoon Degrades Ribbon
1248 Anchorage, Multiquantal Release, and Sound Encoding at the Hair Cell Afferent
1249 Synapse. *J Neurosci* 33: 4456–4467

1250 Johnston S, Parylak SL, Kim S, Mac N, Lim C, Gallina I, Bloyd C, Newberry A, Saavedra CD,
1251 Novak O, *et al* (2021) AAV ablates neurogenesis in the adult murine hippocampus.
1252 *eLife* 10: e59291

1253 Jung S, Maritzen T, Wichmann C, Jing Z, Neef A, Revelo NH, Al-Moyed H, Meese S, Wojcik
1254 SM, Panou I, *et al* (2015) Disruption of adaptor protein 2μ (AP -2μ) in cochlear hair
1255 cells impairs vesicle reloading of synaptic release sites and hearing. *The EMBO*
1256 *Journal* 34: 2686–2702

1257 Kachar B, Brownell WE, Altschuler R & Fex J (1986) Electrokinetic shape changes of cochlear
1258 outer hair cells. *Nature* 322: 365–368

1259 Kalebic N, Gilardi C, Stepien B, Wilsch-Bräuninger M, Long KR, Namba T, Florio M, Langen
1260 B, Lombardot B, Shevchenko A, *et al* (2019) Neocortical Expansion Due to Increased
1261 Proliferation of Basal Progenitors Is Linked to Changes in Their Morphology. *Cell Stem*
1262 *Cell* 24: 535-550.e9

1263 Kalinec F, Holley MC, Iwasa KH, Lim DJ & Kachar B (1992) A membrane-based force
1264 generation mechanism in auditory sensory cells. *Proc Natl Acad Sci USA* 89: 8671–
1265 8675

1266 Kaneko T, Harasztosi C, Mack AF & Gummer AW (2006) Membrane traffic in outer hair cells
1267 of the adult mammalian cochlea. *Eur J of Neuroscience* 23: 2712–2722

1268 Keppeler D, Merino RM, Lopez De La Morena D, Bali B, Huet AT, Gehrt A, Wrobel C,
1269 Subramanian S, Dombrowski T, Wolf F, *et al* (2018) Ultrafast optogenetic stimulation
1270 of the auditory pathway by targeting-optimized Chronos. *The EMBO Journal* 37:
1271 e99649

1272 Kremer JR, Mastronarde DN & McIntosh JR (1996a) Computer Visualization of Three-
1273 Dimensional Image Data Using IMOD. *Journal of Structural Biology* 116: 71–76

1274 Kremer JR, Mastronarde DN & McIntosh JR (1996b) Computer Visualization of Three-
1275 Dimensional Image Data Using IMOD. *Journal of Structural Biology* 116: 71–76

1276 Kutzleb C, Petrasch-Parwez E & Kilimann MW (2006) Cellular and subcellular localization of
1277 paralemmin-1, a protein involved in cell shape control, in the rat brain, adrenal gland
1278 and kidney. *Histochem Cell Biol* 127: 13–30

1279 Kutzleb C, Sanders G, Yamamoto R, Wang X, Lichte B, Petrasch-Parwez E & Kilimann MW
1280 (1998) Paralemmin, a Prenyl-Palmitoyl–anchored Phosphoprotein Abundant in
1281 Neurons and Implicated in Plasma Membrane Dynamics and Cell Process Formation.
1282 *The Journal of Cell Biology* 143: 795–813

1283 Legendre K, Safieddine S, Küssel-Andermann P, Petit C & El-Amraoui A (2008) αII-βV
1284 spectrin bridges the plasma membrane and cortical lattice in the lateral wall of the
1285 auditory outer hair cells. *Journal of Cell Science* 121: 3347–3356

1286 Li Q, Lau A, Morris TJ, Guo L, Fordyce CB & Stanley EF (2004) A Syntaxin 1, $G\alpha_o$, and N-
1287 Type Calcium Channel Complex at a Presynaptic Nerve Terminal: Analysis by
1288 Quantitative Immunocolocalization. *J Neurosci* 24: 4070–4081

1289 Liberman MC, Gao J, He DZZ, Wu X, Jia S & Zuo J (2002) Prestin is required for electromotility
1290 of the outer hair cell and for the cochlear amplifier. *Nature* 419: 300–304

1291 Liu Y, Qi J, Tang, Zhu W, Li H, Tian C, Yang G, Zhang Y, Ni G, He S, *et al* (2019) Critical role
1292 of spectrin in hearing development and deafness. *Science Advances* 5

1293 Lue AJ-C & Brownell WE (1999) Salicylate induced changes in outer hair cell lateral wall
1294 stiffness. *Hearing Research* 135: 163–168

1295 Macarrón-Palacios V, Hubrich J, do Rego Barros Fernandes Lima MA, Metzendorf NG,
1296 Kneilmann S, Trapp M, Acuna C, Patrizi A, D'Este E & Kilimann MW (2025)
1297 Paralemmin-1 controls the nanoarchitecture of the neuronal submembrane
1298 cytoskeleton. *Sci Adv* 11: eadt3724

1299 Meyers C, Alam S, Mane M & Hermonat PL (2001) Altered Biology of Adeno-associated Virus
1300 Type 2 and Human Papillomavirus during Dual Infection of Natural Host Tissue.
1301 *Virology* 287: 30–39

1302 Müller M, Hünerbein KV, Hoidis S & Smolders JWT (2005) A physiological place–frequency
1303 map of the cochlea in the CBA/J mouse. *Hearing Research* 202: 63–73

1304 Nie Y, Chen H, Guo C, Yuan Z, Zhou X, Zhang Y, Zhang X, Mo D & Chen Y (2017)
1305 Palmdelphin promotes myoblast differentiation and muscle regeneration. *Sci Rep* 7:
1306 41608

1307 Oghalai JS, Patel AA, Nakagawa T & Brownell WE (1998) Fluorescence-Imaged
1308 Microdeformation of the Outer Hair Cell Lateral Wall. *J Neurosci* 18: 48–58

1309 Oliver D & Fakler B (1999) Expression density and functional characteristics of the outer hair
1310 cell motor protein are regulated during postnatal development in rat. *J Physiol* 519 Pt
1311 3: 791–800

1312 Oliver D, Hahn H, Antz C, Ruppersberg JP & Fakler B (1998) Interaction of Permeant and
1313 Blocking Ions in Cloned Inward-Rectifier K+ Channels. *Biophysical Journal* 74: 2318–
1314 2326

1315 Orvis J, Gottfried B, Kancherla J, Adkins RS, Song Y, Dror AA, Olley D, Rose K,
1316 Chrysostomou E, Kelly MC, *et al* (2021) gEAR: Gene Expression Analysis Resource
1317 portal for community-driven, multi-omic data exploration. *Nat Methods* 18: 843–844

1318 Pan L, Yan R, Li W & Xu K (2018) Super-Resolution Microscopy Reveals the Native
1319 Ultrastructure of the Erythrocyte Cytoskeleton. *Cell Reports* 22: 1151–1158

1320 Pauli-Magnus D, Hoch G, Strenzke N, Anderson S, Jentsch TJ & Moser T (2007) Detection
1321 and differentiation of sensorineural hearing loss in mice using auditory steady-state
1322 responses and transient auditory brainstem responses. *Neuroscience* 149: 673–684

1323 Peng AW & Ricci AJ (2011) Somatic motility and hair bundle mechanics, are both necessary
1324 for cochlear amplification? *Hearing Research* 273: 109–122

1325 Perkins G, Lee JH, Park S, Kang M, Perez-Flores MC, Ju S, Phillips G, Lysakowski A, Gratton
1326 MA & Yamoah EN (2020) Altered Outer Hair Cell Mitochondrial and Subsurface
1327 Cisternae Connectomics Are Candidate Mechanisms for Hearing Loss in Mice. *J*
1328 *Neurosci* 40: 8556–8572

1329 Rankovic V, Vogl C, Dörje NM, Bahader I, Duque-Afonso CJ, Thirumalai A, Weber T, Kusch
1330 K, Strenzke N & Moser T (2021) Overloaded Adeno-Associated Virus as a Novel Gene
1331 Therapeutic Tool for Otoferlin-Related Deafness. *Front Mol Neurosci* 13: 600051

1332 Raphael RM (2022) Outer hair cell electromechanics as a problem in soft matter physics:
1333 Prestin, the membrane and the cytoskeleton. *Hearing Research* 423: 108426

1334 Rapti K, Stillitano F, Karakikes I, Nonnenmacher M, Weber T, Hulot J-S & Hajjar RJ (2015)
1335 Effectiveness of gene delivery systems for pluripotent and differentiated cells.
1336 *Molecular Therapy - Methods & Clinical Development* 2: 14067

1337 Renier N, Adams EL, Kirst C, Wu Z, Azevedo R, Kohl J, Autry AE, Kadiri L, Umadevi
1338 Venkataraju K, Zhou Y, *et al* (2016) Mapping of Brain Activity by Automated Volume
1339 Analysis of Immediate Early Genes. *Cell* 165: 1789–1802

1340 Revelo NH, Kamin D, Truckenbrodt S, Wong AB, Reuter-Jessen K, Reisinger E, Moser T &
1341 Rizzoli SO (2014) A new probe for super-resolution imaging of membranes elucidates
1342 trafficking pathways. *Journal of Cell Biology* 205: 591–606

1343 Sáinz-Jaspeado M, Smith RO, Plunde O, Pawelzik S-C, Jin Y, Nordling S, Ding Y, Aspenström
1344 P, Hedlund M, Bastianello G, *et al* (2021) Palmdelphin Regulates Nuclear Resilience
1345 to Mechanical Stress in the Endothelium. *Circulation* 144: 1629–1645

1346 Santos-Sacchi J & Tan W (2018) The Frequency Response of Outer Hair Cell Voltage-
1347 Dependent Motility Is Limited by Kinetics of Prestin. *J Neurosci* 38: 5495–5506

1348 Schindelin J, Arganda-Carreras I, Frise E, Kaynig V, Longair M, Pietzsch T, Preibisch S,
1349 Rueden C, Saalfeld S, Schmid B, *et al* (2012) Fiji: an open-source platform for
1350 biological-image analysis. *Nat Methods* 9: 676–682

1351 Schneider CA, Rasband WS & Eliceiri KW (2012) NIH Image to ImageJ: 25 years of image
1352 analysis. *Nat Methods* 9: 671–675

1353 Schulte BA (1993) Immunohistochemical localization of intracellular Ca-ATPase in outer hair
1354 cells, neurons and fibrocytes in the adult and developing inner ear. *Hearing Research*
1355 65: 262–273

1356 Seymour ML, Rajagopalan L, Duret G, Volk MJ, Liu H, Brownell WE & Pereira FA (2016)
1357 Membrane prestin expression correlates with the magnitude of prestin-associated
1358 charge movement. *Hearing Research* 339: 50–59

1359 Shehata WE, Brownell WE & Dieler R (1991) Effects of Salicylate on Shape, Electromotility
1360 and Membrane Characteristics of Isolated Outer Hair Cells from Guinea Pig Cochlea.
1361 *Acta Oto-Laryngologica* 111: 707–718

1362 Shotton DM, Burke BE & Branton D (1979) The molecular structure of human erythrocyte
1363 spectrin. *Journal of Molecular Biology* 131: 303–329

1364 Song L & Santos-Sacchi J (2015) An Electrical Inspection of the Subsurface Cisternae of the
1365 Outer Hair Cell. *Biophysical Journal* 108: 568–577

1366 Spoendlin H (1966) The organization of the cochlear receptor. *Fortschr Hals Nasen*
1367 *Ohrenheilkd* 13: 1–227

1368 Steyger PS, Furness DN, Hackney CM & Richardson GP (1989) Tubulin and microtubules in
1369 cochlear hair cells: Comparative immunocytochemistry and ultrastructure. *Hearing*
1370 *Research* 42: 1–16

1371 Strenzke N, Chakrabarti R, Al-Moyed H, Müller A, Hoch G, Pangrsic T, Yamanbaeva G, Lenz
1372 C, Pan K, Auge E, *et al* (2016) Hair cell synaptic dysfunction, auditory fatigue and
1373 thermal sensitivity in otoferlin Ile515Thr mutants. *The EMBO Journal* 35: 2519–2535

1374 Sturm AK, Rajagopalan L, Yoo D, Brownell WE & Pereira FA (2007) Functional expression
1375 and microdomain localization of prestin in cultured cells. *Otolaryngol--head neck surg*
1376 136: 434–439

1377 Triffo WJ, Palsdottir H, Song J, Morgan DG, McDonald KL, Auer M & Raphael RM (2019) 3D
1378 Ultrastructure of the Cochlear Outer Hair Cell Lateral Wall Revealed By Electron
1379 Tomography. *Front Cell Neurosci* 13: 560

1380 Voorn RA, Sternbach M, Jarysta A, Rankovic V, Tarchini B, Wolf F & Vogl C (2024) Slow
1381 kinesin-dependent microtubular transport facilitates ribbon synapse assembly in
1382 developing cochlear inner hair cells. doi:10.7554/eLife.98145.1 [PREPRINT]

1383 Wada H, Kimura K, Gomi T, Sugawara M, Katori Y, Kakehata S, Ikeda K & Kobayashi T (2004)
1384 Imaging of the cortical cytoskeleton of guinea pig outer hair cells using atomic force
1385 microscopy. *Hearing Research* 187: 51–62

1386 Wei G, Qiu S, Gao X, Zheng L, Chen Y, Ma Y, Feng H, Yang J, Dong G, Nie H, *et al* (2025)
1387 Single Administration of AAV-m *Atp6v1b2* Gene Therapy Rescues Hearing and

Vestibular Disorders Caused by *Atp6v1b2* -Induced Lysosomal Dysfunction in Hair Cells. *Advanced Science*: 2408878

Wong AB, Rutherford MA, Gabrielaitis M, Pangršič T, Göttfert F, Frank T, Michanski S, Hell S, Wolf F, Wichmann C, *et al* (2014) Developmental refinement of hair cell synapses tightens the coupling of Ca^{2+} influx to exocytosis. *EMBO J*: n/a-n/a

Yao Q, Wang H, Chen H, Li Z, Jiang Y, Li Z, Wang J, Xing Y, Liu F, Yu D, *et al* (2022) Essential Role of Sptan1 in Cochlear Hair Cell Morphology and Function Via Focal Adhesion Signaling. *Mol Neurobiol* 59: 386–404

Zanta-Boussif MA, Charrier S, Brice-Ouzet A, Martin S, Opolon P, Thrasher AJ, Hope TJ & Galy A (2009) Validation of a mutated PRE sequence allowing high and sustained transgene expression while abrogating WHV-X protein synthesis: application to the gene therapy of WAS. *Gene Ther* 16: 605–619

Zheng J, Du G-G, Matsuda K, Orem A, Aguiñaga S, Deák L, Navarrete E, Madison LD & Dallos P (2005) The C-terminus of prestin influences nonlinear capacitance and plasma membrane targeting. *Journal of Cell Science* 118: 2987–2996

Zheng J, Shen W, He DZZ, Long KB, Madison LD & Dallos P (2000) Prestin is the motor protein of cochlear outer hair cells. *Nature* 405: 149–155

Zhong G, He J, Zhou R, Lorenzo D, Babcock HP, Bennett V & Zhuang X (2014) Developmental mechanism of the periodic membrane skeleton in axons. *eLife* 3: e04581

Main Figures

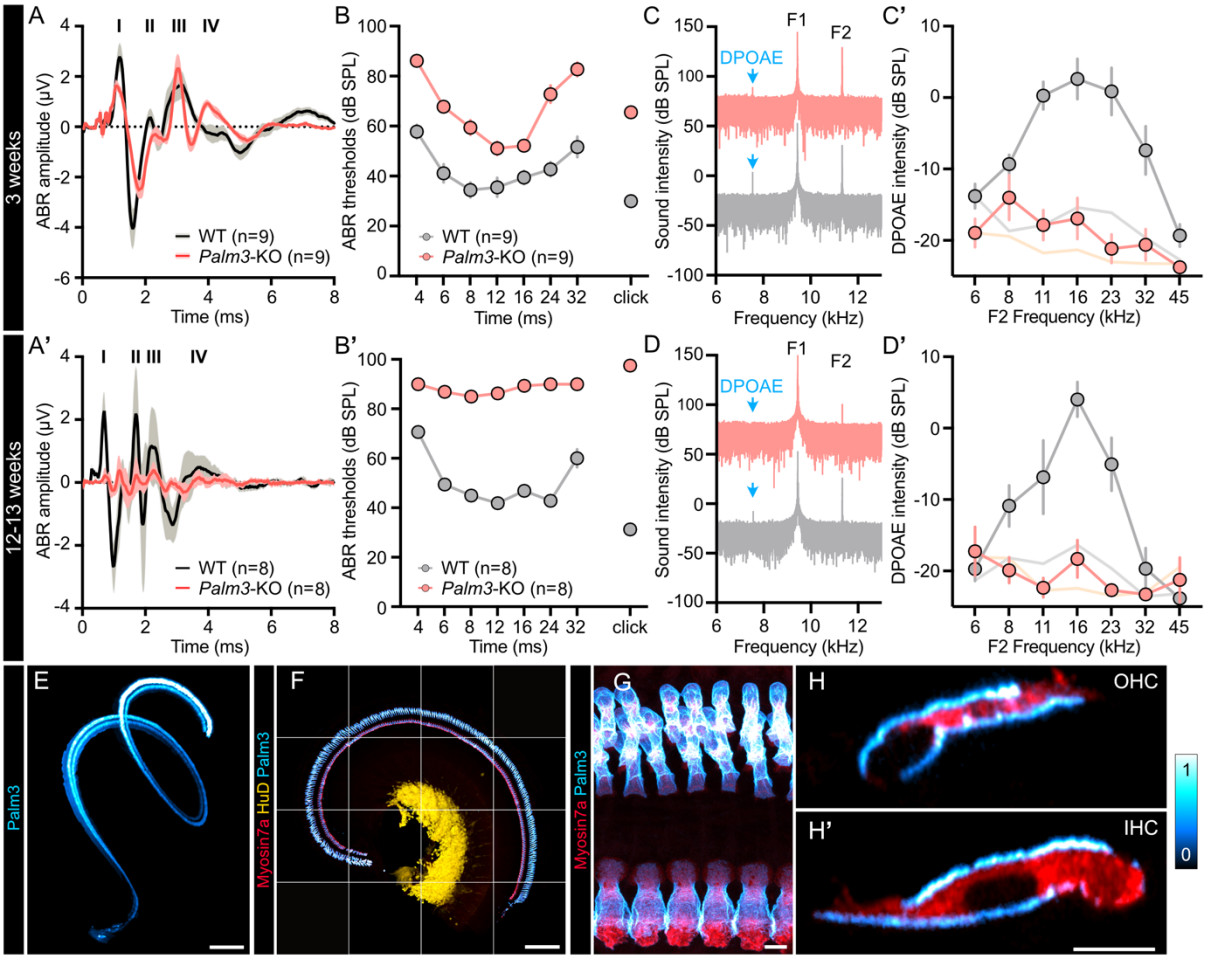

Figure 1. Palm3-KO mice exhibit early onset and progressive hearing loss.

(A,A') Grand averages of auditory brainstem response (ABR) waveforms upon 100 dB SPL click stimulation at 20 Hz showed (A) a moderate amplitude reduction in 3-week-old and (A') a stark reduction in 12-13-week-old *Palm3*-KO mice compared to WT-littermates.

(B,B') ABR threshold measurements from (B) 3-week- ($N_{animals}$= 9 for each WT and *Palm3*-KO) and (B') 12-13-week-old ($N_{animals}$= 8 for each WT and *Palm3*-KO) WT (grey) and *Palm3*-KO (pink) mice revealed early-onset and progressive hearing impairment in *Palm3*-KO mice. Tone burst threshold values that surpassed the maximum output of the loudspeaker of 80 dB SPL were assigned as 90 dB for the purpose of calculating means ± SEM.

(C,D) Representative frequency spectra of DPOAE recordings for the specified age groups for the stimulus combination F1 9.4 kHz 60 dB, F2 11.3 kHz 50 dB, expected DPOAE at 7.5kHz. *Palm3*-KO traces are offset by +100 dB to avoid overlap. Note the complete absence of a detectable DPOAE in the 12-13-week-old cohort.

1424 (C',D') DPOAE amplitude in response to paired simultaneous sine waves in (C') 3-week- ($N_{animals}$= 9 for
1425 WT and $N_{animals}$= 8 for *Palm3*-KO) and (D') 12-13-week-old ($N_{animals}$= 7 for each WT and *Palm3*-KO)
1426 *Palm3*-KO (pink) mice are attenuated compared to WT littermates (grey). Light grey and light orange
1427 lines indicate the average noise floor.
1428 (E) Representative maximum z-projection of lightsheet microscopy on iDisco-cleared cochlea of a P14
1429 WT mouse. Hair cells are stained with Palm3 (cyan hot). Lightsheet microscopy image was processed
1430 as described in **Supplementary figure 2**. Scale bar: 100 µm.
1431 (F) Representative maximum z-projection showing an overview of the distribution of Palm3 expression
1432 in the organ of Corti from a P16 WT mouse. Hair cells are immunostained for Palm3 (cyan hot) and
1433 Myosin7A (red), SGN somata are immunostained for HuD (yellow). Scale bar: 150 µm.
1434 (G) Localization of Palm3 to the lateral plasma membrane of auditory hair cells at 100X magnification,
1435 assessed in the apical cochlear turns of a P16 WT mouse. Scale bar: 5 µm.
1436 (H-H') Representative yz- projections of single optical sections of an OHC and an IHC. Scale bar: 5 µm.
1437
1438 Data information: Comparison of genotypes: Two-way ANOVA with Holm-Šídák's multiple comparisons
1439 correction: ****P <0.0001; Mean ± SEM.
1440
1441

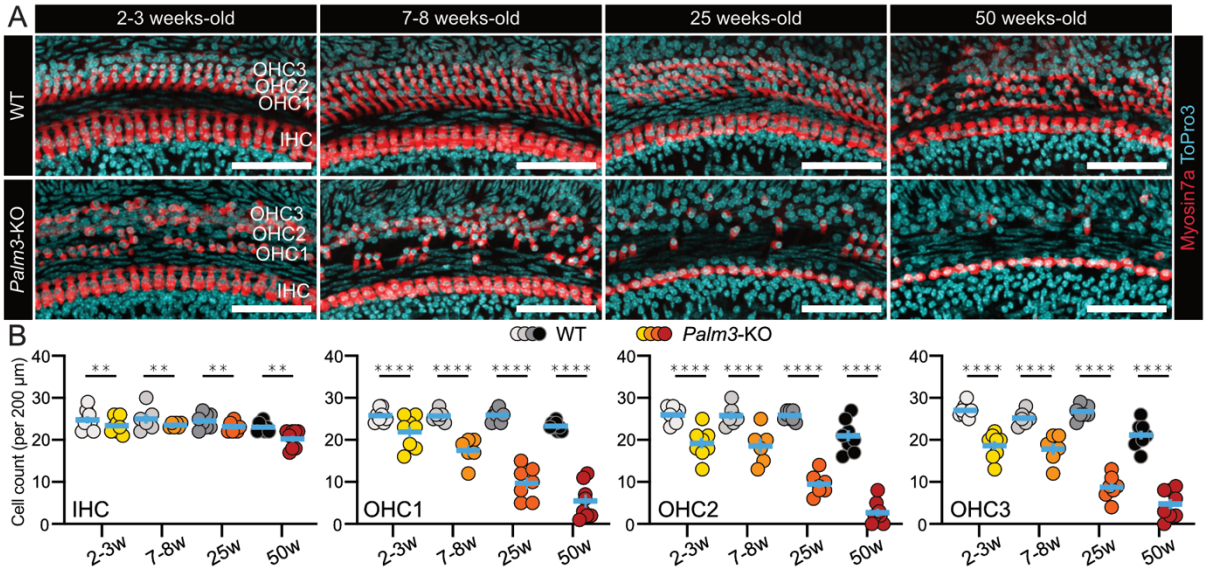

Figure 2. Hearing loss in Palm3-KO is due to progressive hair cell degeneration.

(A) Hair cell survival was assessed in the apical cochlear turn (8-11 kHz frequency range) of 2-3 week-, 7-8 week- , 25 week- and 50-week-old WT (upper panels) and *Palm3*-KO animals (lower panels). Organs of Corti explants were immunostained against the hair cell marker Myosin7a (red) and the DNA stain ToPro3 (cyan). Scale bars: 50 µm.

(B) Quantitative assessment of hair cell counts in whole-mount apical organs of Corti revealed *Palm3*-KO mice show a small decrease in the survival rate of IHCs, whereas OHCs show varying degrees of progressive degeneration in respect to the different rows. 2-3 weeks old: $N_{animals}$= 4, n_{Corti} = 8 for each WT and *Palm3*-KO, 7-8 weeks old: $N_{animals}$= 3, n_{Corti} = 6 for each WT and *Palm3*-KO, 25 weeks old: $N_{animals}$= 4, n_{Corti} = 8 for WT and $N_{animals}$= 4, n_{Corti} = 7 for *Palm3*-KO, 50 weeks old: $N_{animals}$= 4, n_{Corti} = 8 for each WT and *Palm3*-KO.

Data information: Two-way ANOVA with Holm-Šídák's multiple comparisons correction: $^{**}P$ <0.01; $^{****}P$ <0.0001; Mean ± SEM.

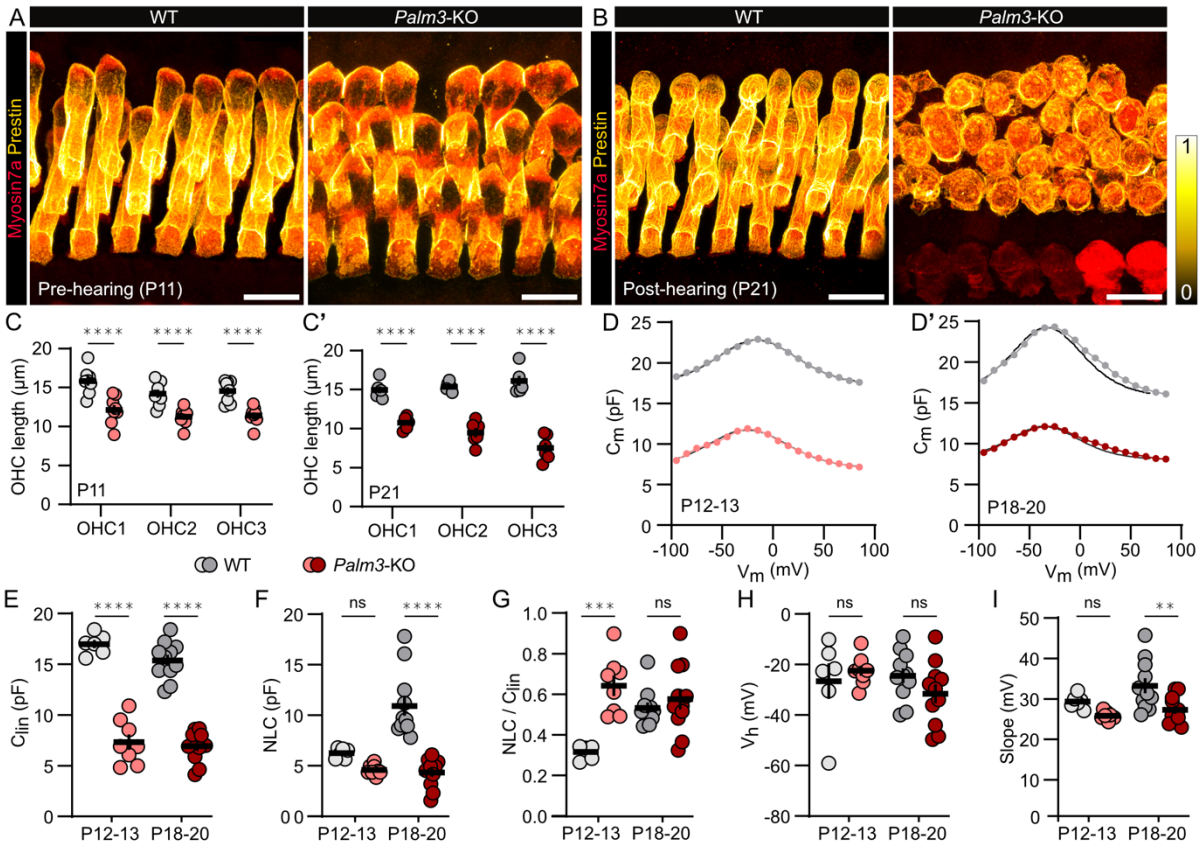

Figure 3. Genetic loss of Palm3 resulted in reduced OHC length, perturbed localization of Prestin and decreased electromotile capacity.

(A,B) Representative confocal z-y projections of apical organs of Corti from WT and *Palm3*-KO at (A) P11 and (B) P21. OHCs were immunostained against the hair cell marker Myosin7a (red) and Prestin (yellow hot). Scale bars: 10 µm.

(C,C') *Palm3*-KO organs of Corti reveal a dramatic reduction in OHC lengths regardless of row position at (C) P11 ($N_{animals}$= 4, n_{Corti} = 8 for WT and $N_{animals}$= 4, n_{Corti} = 8 for *Palm3*-KO), which progressed until (C') P21 ($N_{animals}$= 3, n_{Corti} = 6 for WT and $N_{animals}$= 3, n_{Corti} = 6 for *Palm3*-KO).

(D-D') Example traces of voltage-dependent cell capacitance from (D) P12-13 and (D') P18-20 WT and *Palm3*-KO OHCs measured with the stair-step stimulus protocol from -100 mV to 85 mV in 10-mV increments and 5 ms step duration.

(E-I) Quantitative analysis derived from (D,D') shows *Palm3*-KO OHCs to have (E) an overall decrease in linear capacitance (C_{lin}), (F) reduced non-linear capacitance (NLC) at P18-20, (G) increased ratio of NLC to C_{lin} (NLC/ C_{lin}) at P12-13, (H) unchanged voltage at peak capacitance (V_h), and (I) decreased slope at P18-20. P12-13: n_{cells} = 6 for WT and n_{cells} = 8 for *Palm3*-KO; P18-20: n_{cells} = 11 for WT and n_{cells} = 9 for *Palm3*-KO.

Data information: Two-way ANOVA with Holm-Šídák's multiple comparisons correction: ns = not significant; ** $P < 0.01$; *** $P < 0.001$ **** $P < 0.0001$; Mean ± SEM.

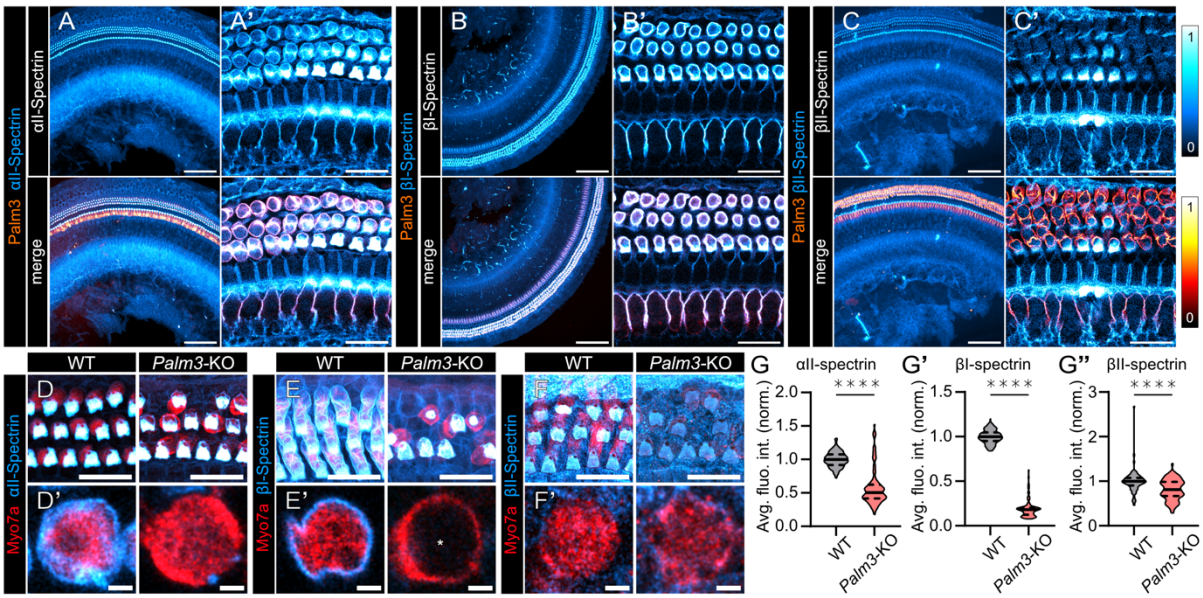

Figure 4. Loss of Palm3 reduces spectrin abundance at OHC lateral plasma membranes.

(A-C') Representative confocal maximum z-projections showing localization of Palm3 (red hot) and either αII-Spectrin, βI-Spectrin or βII-Spectrin (cyan hot) within the organ of Corti. (A,B,C) Overview images are depicted on the left columns (scale bars: 100 µm), whereas (A',B',C') right columns show single optical sections of the respective staining at higher magnification (scale bars: 20 µm).

(D-F') Representative confocal maximum z- projections of OHCs stained against Myosin7a (red) and either αII-Spectrin, βI-Spectrin or βII-Spectrin (cyan hot) from 6-week-old WT and *Palm3*-KO. (D,E,F) Upper panels show overview of the OHC rows and (D',E',F') lower panels show single optical sections of individual OHCs of the respective stacks. Scale bars: upper panels: 20 µm, lower panels: 2 µm. The * in E' indicates the unstained nucleus.

(G-G") Violin plots showing average fluorescence intensity of (G) αII-Spectrin ($N_{animals}$= 5, n_{Corti} = 10, n_{OHC} = 134 for WT and $N_{animals}$= 5, n_{Corti} = 10, n_{OHC} = 90 for *Palm3*-KO), (G') βI-Spectrin ($N_{animals}$= 5, n_{Corti} = 10, n_{OHC} = 130 for WT and $N_{animals}$= 5, n_{Corti} = 10, n_{OHC} = 88 for *Palm3*-KO) and (G") βII-Spectrin ($N_{animals}$= 3, n_{Corti} = 6, n_{OHC} = 71 for WT and $N_{animals}$= 3, n_{Corti} = 6, n_{OHC} = 68 for *Palm3*-KO) along the OHC lateral wall is decreased in absence of Palm3.

Data information: Two-tailed Mann-Whitney test: **** $P < 0.0001$.

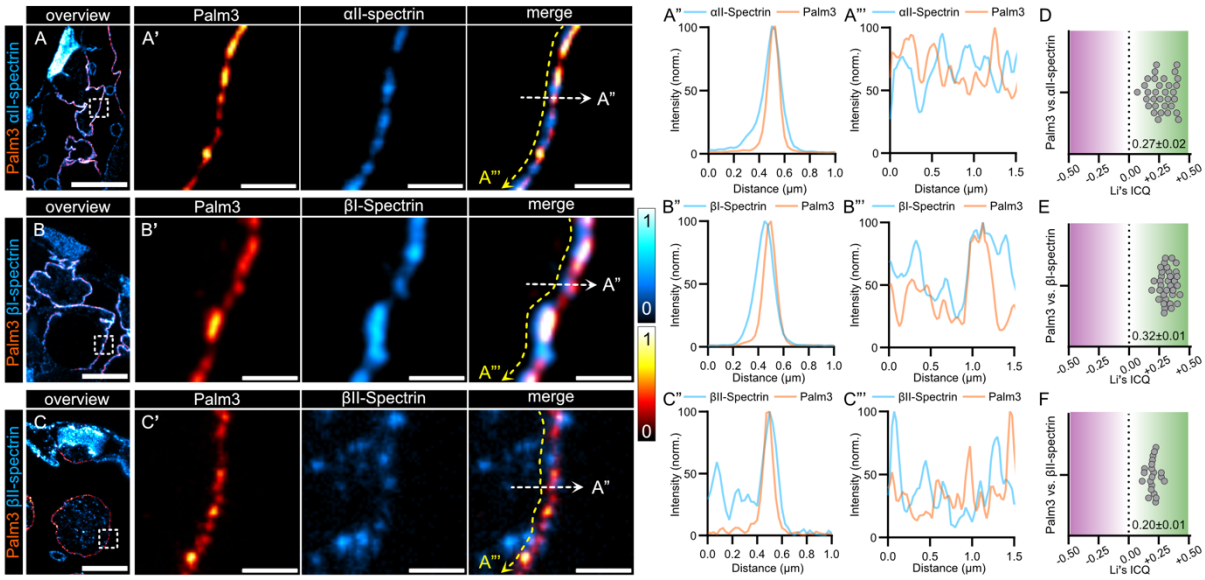

Figure 5. Localization of Palm3 and different spectrin isoforms in the OHC lateral plasma membrane.

(A-C) Two-color 2D-STED IF images of ~80-90 nm ultrathin melamine-embedded sections of organs of Corti from 6-8-week-old WT mice, showing a single OHC labeled with Palm3 (red hot) and either (A) αII-Spectrin, (B) βI-Spectrin, or (C) βII-Spectrin (cyan hot). Scale bars: 5 µm.

(A'-C') Close-up views of insets depicted in (A-C), showing a region of interest in the OHC lateral plasma membrane labeled with Palm3 (red hot) and either (A') αII-Spectrin, (B') βI-Spectrin, or (C') βII-Spectrin (cyan hot). Dotted line arrows indicate the starting and end point of the intensity profile analyses shown in (A"-C" and A'''-C'''). Scale bars: 0.5 µm.

(A"-C") Transverse intensity profiles of Palm3 (orange) and either (A") αII-Spectrin, (B") βI-Spectrin, or (C") βII-Spectrin (blue).

(A'''-C''') Longitudinal intensity profiles of Palm3 (orange) and either (A''') αII-Spectrin, (B''') βI-Spectrin, or (C''') βII-Spectrin (blue).

(D-F) Scattered dot plots showing Li's intensity correlation quotient (ICQ) values highlights the spatial correlation between Palm3 and either (D) αII-Spectrin ($N_{animals}$= 3, n_{images}= 32), (E) βI-Spectrin ($N_{animals}$= 3, n_{images}= 34), or (F) βII-Spectrin ($N_{animals}$= 2, n_{images}= 21). Mean ± SEM values are depicted in the Figure.

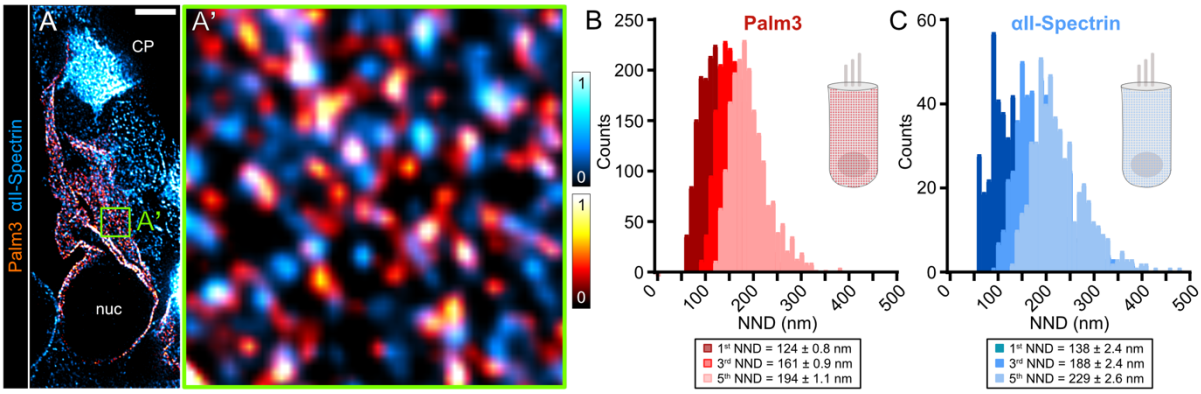

Figure 6. Spatial distribution of Palm3 and αII-Spectrin within the OHC lateral plasma membrane

(A,A') Representative two-color 2D-STED IF images of ~80-90 nm ultrathin melamine-embedded sections of Palm3-stained organs of Corti from 6-8-week-old WT mice, showing (A) a single OHC and (A') a close up view of the inset depicted in (A) labeled with Palm3 (red hot) and αII-Spectrin (cyan hot). Scale bar in (A) 2 µm, box width in (A') 1.5x1.5 µm.

(B) First to fifth NNDs between Palm3 immunostaining puncta. Inset shows the mean NND value for each configuration. $N_{animals}$= 4; n_{images}= 9; for 1st NND: n_{Palm}= 1965, for 3rd NND: n_{Palm}= 1966, and for 5th NND: n_{Palm}= 1966.

(C) First to fifth NNDs between αII-Spectrin immunostaining puncta. Inset shows the mean NND value for each configuration. $N_{animals}$= 4; n_{images}= 9; for 1st, 3rd, 5th NND: $n_{\alpha II\text{-}Spectrin}$= 504.

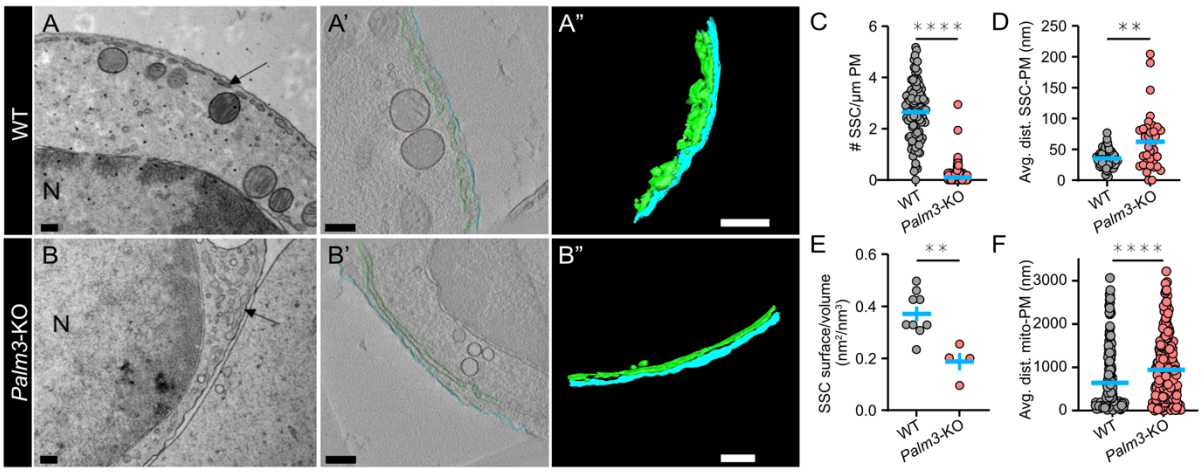

Figure 7. Palm3-KO subsurface cisternae (SSC) are fewer in number, structurally less complex and located more distally from the lateral plasma membrane.

(A-B) Representative transmission electron microscopy (TEM) micrograph of (A) WT and (B) *Palm3*-KO OHC lateral wall obtained after high pressure freezing/freeze-substitution from P14 mice. N indicates the cell nucleus and arrow indicates SSCs. Scale bars: 0.2 µm.

(A'-B") Representative virtual electron tomographic sections with their (A",B") corresponding 3D models of (A',A") WT and (B',B") *Palm3*-KO OHC lateral wall obtained after high pressure freezing/freeze-substitution from P14 mice. The tomographic reconstructions show the OHC plasma membrane in cyan and SSC in green. Scale bars: 0.2 µm.

(C-E) Scattered dot plots display the quantification of (C) number of SSC per µm membrane ($N_{animals}$= 2, n_{OHCs} = 23, $n_{measurements}$= 102 for WT and $N_{animals}$= 5, n_{OHCs} = 30, $n_{measurements}$= 165 for *Palm3*-KO), (D) average distance of SSC to the plasma membrane (PM) ($N_{animals}$= 2, n_{OHCs} = 23, $n_{measurements}$= 81 for WT and $N_{animals}$= 2, n_{OHCs} = 21, $n_{measurements}$= 36 for *Palm3*-KO), and (E) surface per volume mesh membrane ($N_{animals}$= 2, n_{OHCs} = 23, $n_{measurements}$= 9 for WT and $N_{animals}$= 2, n_{OHCs} = 21, $n_{measurements}$= 4 for *Palm3*-KO). Blue bars represent mean ± SEM.

(F) Average distance of mitochondria to the plasma membrane is increased in *Palm3*-KO OHCs ($N_{animals}$= 2, n_{OHCs} = 23, $n_{measurements}$= 230 for WT and $N_{animals}$= 2, n_{OHCs} = 21, $n_{measurements}$= 255 for *Palm3*-KO).

Data information: Two-tailed Mann-Whitney test: ** $P < 0.01$, **** $P < 0.0001$; Mean ± SEM.

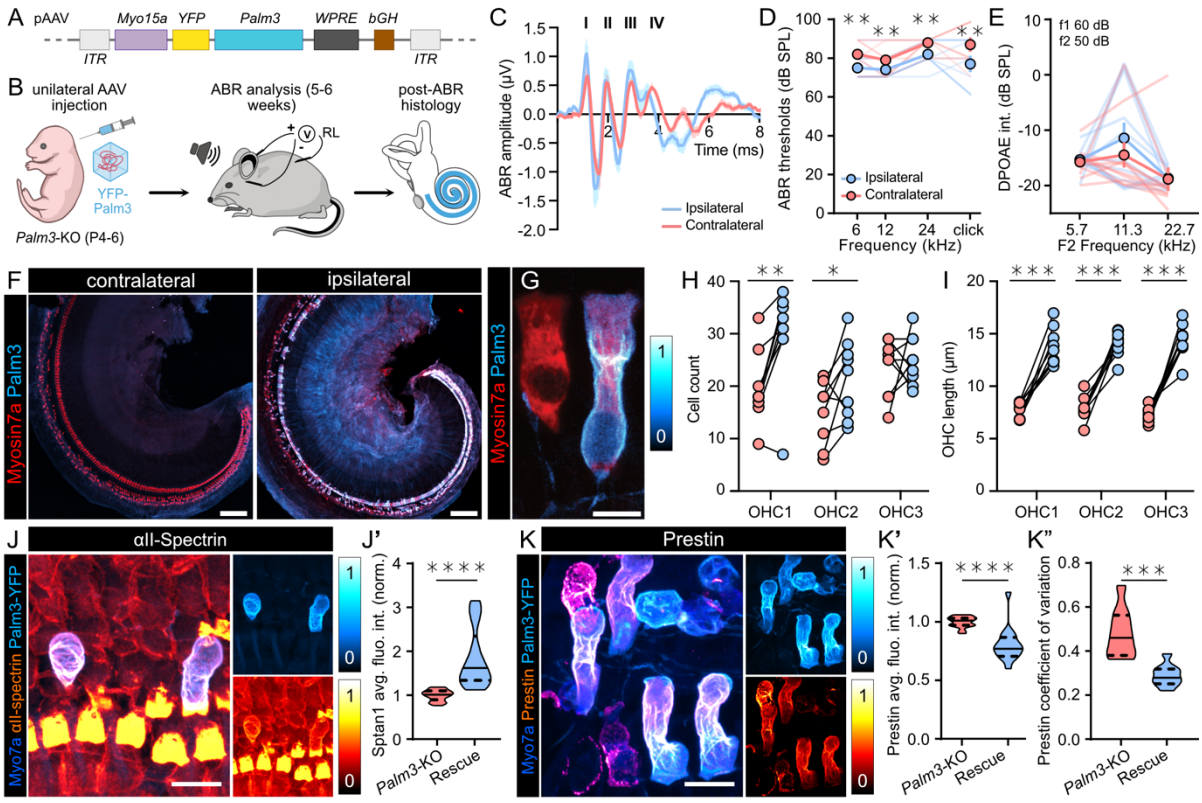

Figure 8. AAV-mediated rescue improved hearing function and restored OHC counts and lengths in Palm3-KO mice.

(A) The vector is based on a pAAV backbone and carries the mouse *Palm3* gene fused to a yellow fluorescent protein gene (*YFP*). This fusion construct is inserted between the human *Myo15a* promoter and a non-oncogenic variant of Woodchuck hepatitis virus posttranslational regulatory element (*WPRE*), followed by the bovine growth hormone (*bGH*) polyadenylation signal sequences. The entire cassette is flanked by inverted terminal repeats (*ITR*s).

(B) Schematic overview of the AAV-mediated Palm3 rescue experimental procedure. *AAV.S_Myo15a_YFP-Palm3* was administered via round window intracochlear injection at P4-6 in Palm3-KO mouse pups. After the injection, ABR and DPOAE measurements were performed to evaluate hearing function following a maturation period of 4 to 5 weeks. Subsequently, the animals were sacrificed, and their cochleae harvested for morphological assessment.

(C) Grand averages of ABR waveforms upon 100 dB and 20 Hz click stimulation in 5-week-old *Palm3*-KO mice following injection of *AAV.S_Myo15a_YFP-Palm3* in ipsilateral ears (blue) and non-injected contralateral ears (pink) of the same animals. Averages represented by lines, means ± SEM

1566 represented by shaded areas, ABR waves generated along the auditory pathway represented by roman
1567 numerals (Jewett Waves I-V).
1568 (D) ABR thresholds to clicks and 6, 12, and 24 kHz tone bursts in injected and contralateral ears
1569 ($N_{animals}$= 10, with n_{Corti} = 10 for ipsilateral and n_{Corti} = 10 for contralateral; Two-way ANOVA with Holm-
1570 Šídák‘s multiple comparisons correction: ** $P < 0.01$; Mean ± SEM).
1571 (E) Slight increase in DPOAE amplitude at f2 frequency of 11.3 kHz suggests a subtle improvement of
1572 amplification in *Palm3*-rescue. Orange and light blue lines indicate the average noise floor ($N_{animals}$= 10,
1573 with n_{Corti} = 10 for ipsilateral and n_{Corti} = 10 for contralateral; Two-way ANOVA with Holm-Šídák‘s multiple
1574 comparisons correction: $P = 0.6225$; Mean ± SEM).
1575 (F) Representative confocal maximum z-projections of whole-mount apical turns of non-injected
1576 (contralateral-) and injected (ipsilateral) ears of 5-week- old *Palm3*-KO animals. Cortis were stained for
1577 Myosin7a (red) and Palm3-YFP (cyan hot). Scale bars: 100 µm.
1578 (G) A *Palm3*-transduced OHC displays improved cellular morphology in comparison to a neighboring
1579 non-transduced OHC. Cortis stained for Myosin7a (red) and Palm3-YFP (cyan hot). Scale bar: 10 µm.
1580 (H) Single value plots showing OHCs counts within a 300 µm x 300 µm region of interest to exhibit a
1581 trend toward increased survival in *Palm3*-rescue ears ($N_{animals}$= 9, with n_{Corti} = 9 for ipsilateral and n_{Corti}
1582 = 9 for contralateral: Two-way ANOVA with Holm-Šídák‘s multiple comparisons correction: ns = not
1583 significant; * $P < 0.05$; ** $P < 0.01$; Mean ± SEM; connecting lines identify individual animals).
1584 (I) *Palm3*-transduced OHCs show restored cell lengths in all three OHC rows ($N_{animals}$= 9, with n_{Corti} = 9
1585 for ipsilateral and n_{Corti} = 9 for contralateral; Two-way ANOVA with Holm-Šídák‘s multiple comparisons
1586 correction: **** $P < 0.0001$; Mean ± SEM).
1587 (J) Representative confocal maximum z-projections of OHCs in AAV-injected, 5-week-old *Palm3*-KO
1588 animals (n = 5). OHCs were stained with Myosin7a (blue), Palm3 (cyan hot), and αII-Spectrin (red hot).
1589 Scale bars: 5 µm.
1590 (J’) Violin plot showing normalized average fluorescence intensity of αII-Spectrin revealed restored αII-
1591 Spectrin-labeling intensity in *Palm3*-transduced OHCs ($N_{animals}$= 5, with n_{OHCs} = 27 for Palm3-negative
1592 and n_{OHCs} = 25 for Palm3-positive; Two-tailed Mann-Whitney test: **** P < 0.0001; Mean ± SEM).
1593 (K) OHCs were stained with Myosin7a (blue), Palm3 (cyan hot), and Prestin (red hot). Representative
1594 confocal maximum z-projections of OHCs in AAV-injected, 5-week-old *Palm3*-KO animals (n = 5). Scale
1595 bars: 5 µm.

1596 (K') Violin plot showing normalized average fluorescence intensity of Prestin revealed decreased
1597 Prestin-labeling intensity in *Palm3*-transduced OHCs. ($N_{animals}$= 4, with n_{OHCs} = 17 for Palm3-negative
1598 and n_{OHCs} = 15 for Palm3-positive; Two-tailed Mann-Whitney test: **** P < 0.0001; Mean ± SEM).
1599 (K") Coefficient of variation of Prestin-labeling intensity indicates a restoration of homogeneous Prestin
1600 distribution over the lateral membrane of OHCs in *Palm3*-transduced OHCs. ($N_{animals}$= 4, with n_{OHCs} =
1601 17 for Palm3-negative and n_{OHCs} = 15 for Palm3-positive; Two-tailed Mann-Whitney test: *** P < 0.001;
1602 Mean ± SEM).
1603
1604